



Inferring Explosion Properties from Type II-Plateau Supernova Light Curves

Jared A. Goldberg¹ , Lars Bildsten^{1,2}, and Bill Paxton²

¹Department of Physics, University of California, Santa Barbara, CA 93106, USA; goldberg@physics.ucsb.edu

²Kavli Institute for Theoretical Physics, University of California, Santa Barbara, CA 93106, USA

Received 2019 March 21; revised 2019 May 13; accepted 2019 May 17; published 2019 June 26

Abstract

We present advances in modeling Type IIP supernovae (SNe IIP) using MESA for evolution to shock breakout coupled with STELLA for generating light and radial velocity curves. Explosion models and synthetic light curves can be used to translate observable properties of SNe (such as the luminosity at day 50 and the duration of the plateau, as well as the observable quantity ET, defined as the time-weighted integrated luminosity that would have been generated if there were no ⁵⁶Ni in the ejecta) into families of explosions that produce the same light curve and velocities on the plateau. These predicted families of explosions provide a useful guide toward modeling observed SNe and can constrain explosion properties when coupled with other observational or theoretical constraints. For an observed SN with a measured ⁵⁶Ni mass, breaking the degeneracies within these families of explosions (ejecta mass, explosion energy, and progenitor radius) requires independent knowledge of one parameter. We expect the most common case to be a progenitor radius measurement for a nearby SN. We show that ejecta velocities inferred from the Fe II λ 5169 line measured during the majority of the plateau phase provide little additional information about explosion characteristics. Only during the initial shock cooling phase can photospheric velocity measurements potentially aid in unraveling light-curve degeneracies.

Key words: hydrodynamics – radiative transfer – stars: massive – supernovae: general

1. Introduction

Through an expanding network of ground- and space-based telescopes, the astrophysical community has an unprecedented ability to probe transient events. Along with a host of facilities, such as the All Sky Automated Survey for Supernovae (ASAS-SN; Kochanek et al. 2017), the Las Cumbres Observatory (Brown et al. 2013) is building the largest set of data ever collected on all nearby supernova (SN) events. Some SNe discovered have known progenitors in distant galaxies (Smartt 2009). And the data are improving—the Zwicky Transient Facility (Bellm et al. 2019) has begun discovering multiple SNe on a nightly basis, and the Large Synoptic Survey Telescope (LSST Science Collaboration et al. 2009) will revolutionize time-domain astronomy with repeated nightly imaging of the entire sky with outstanding spatial resolution.

In this paper we focus on SNe IIP, core-collapse events of dying massive stars ($M > 10M_{\odot}$) that yield distinctive light curves that plateau over a period of ≈ 100 days. The duration and brightness of these light curves reflect the progenitor’s radius (R), ejected mass (M_{ej}), energy of the explosion (E_{exp}), and ⁵⁶Ni mass (M_{Ni}). Inferring these properties from the observations has broad applications. Extracting progenitor information from SN observations could lend insight into which stars explode as SNe and which collapse directly into black holes. It would also have implications for the missing red supergiant (RSG) problem identified by Smartt (2009) and updated by Smartt (2015), whereby SNe II with known progenitors seem to come from explosions of RSGs with initial masses of $M_{\text{ZAMS}} < 17M_{\odot}$, whereas evolutionary models have a cutoff mass of around $30M_{\odot}$.

Our understanding has benefitted from three-dimensional modeling of light curves and spectroscopic data for specific Type IIP events, such as the work of Wongwathanarat et al. (2015) and Utrobin et al. (2017), as well as 3D simulations that probe specific regions of parameter space of these SNe (e.g.,

Burrows et al. 2019). Although 3D models are incredibly useful for describing specific systems and probing specific regions of the possible parameter space of progenitors and their explosions, substantial effort is required to estimate the parameters of a single observed explosion. The computational demand for individual 3D calculations presents a challenge for probing the parameter space of possible progenitor models for a large ensemble of explosions.

Here we utilize the open-source one-dimensional stellar evolution software instrument, Modules for Experiments in Stellar Astrophysics (MESA; Paxton et al. 2011, 2013, 2015, 2018, 2019), to model an ensemble of SN IIP progenitors, interfacing with the radiative transfer code STELLA (Blinnikov et al. 1998, 2006; Blinnikov & Sorokina 2004; Baklanov et al. 2005) to simulate their light curves and photospheric evolution. We include the effects of the Duffell (2016) prescription for mixing via the Rayleigh–Taylor instability, which allows for significant mixing of important chemical species such as ⁵⁶Ni and yields a more realistic density and temperature profile in the ejecta at shock breakout (Paxton et al. 2018, MESA IV).

The increasing abundance of data has led to a new approach to understanding Type IIP progenitors and explosions in an ensemble fashion. Pejcha & Prieto (2015a, 2015b) and Müller et al. (2017) took such an approach, characterizing a total of 38 SNe IIP by their luminosity and duration of the plateau, as well as the velocity at day 50 as inferred via the Fe II λ 5169 line. By fitting these three measurements to the analytics of Popov (1993)³ and early numerics of Litvinova & Nadyozhin (1983), these authors inferred M_{ej} , E_{exp} , and R from these observables. To this end, we show that MESA+STELLA reproduces a scaling for plateau luminosity at day 50, L_{50} , similar to that of Popov (1993), and we introduce new best-fit scaling laws for L_{50} and for the duration of the plateau t_p in the limit of

³ See also the update by Sukhbold et al. (2016) to the Kepler+Sedona results of Kasen & Woosley (2009), which find similar scalings.

Table 1
Properties of Our RSG Progenitor Models at the Time of the Explosion

Model	M_{ZAMS} (M_{\odot})	M_{final} (M_{\odot})	$M_{\text{c},i}$ (M_{\odot})	$M_{\text{He core}}$ (M_{\odot})	M_{ej} (M_{\odot})	M_{env} (M_{\odot})	$\omega/\omega_{\text{crit}}$	$ E_{\text{bind}} $ (10^{50} erg)	T_{eff} (K)	$\log(L_{\text{prog}}/L_{\odot})$	R (R_{\odot})
M9.3_R433*	11.8	10.71	1.44	3.58	9.28	7.13	0.2	1.39	4370	4.79	433
M11.3_R541*	13.0	12.86	1.57	4.22	11.29	8.65	0.0	2.65	4280	4.95	541
M12.9_R766*	16.0	14.46	1.58	5.44	12.88	9.02	0.2	4.45	3960	5.11	766
M16.3_R608*	19.0	17.79	1.51	5.72	16.29	12.07	0.2	1.29	4490	5.13	608
M15.7_R800*	19.0	17.33	1.66	6.83	15.67	10.50	0.2	2.39	4040	5.18	800
M15.0_R1140*	19.0	16.77	1.78	7.55	14.99	9.22	0.2	3.31	3660	5.32	1140
M20.8_R969	25.0	22.28	1.77	8.85	20.76	13.43	0.0	8.45	4870	5.68	969
M9.8_R909	13.7	11.36	1.60	7.75	9.8	3.61	0.2	1.81	2380	4.99	909
M10.2_R848	13.5	11.99	1.77	4.24	10.22	7.75	0.2	1.92	3510	5.13	848
M17.8_R587	20.0	19.41	1.62	7.23	17.79	12.18	0.0	2.41	5480	5.44	587

Note. Models indicated by an asterisk are part of our standard suite, upon which the majority of our analysis is based. $M_{\text{c},i}$ is the mass of the excised core, and $M_{\text{He core}}$ is the He core mass in the pre-explosion model. Names are determined by the ejecta mass and radius of each progenitor model at shock breakout, $M < M_{\text{ej}} > R < R >$.

^{56}Ni -rich events. We also discuss the relationship between our model properties and the observable ET, the time-weighted integrated luminosity that would have been generated if there was no ^{56}Ni in the ejecta (Nakar et al. 2016; Shussman et al. 2016a), and show how ET can also be used to provide similar constraints on explosion properties. As an observable, ET is defined by Equations (14) and (15). Additionally, we show that the measured velocity at day 50 from the Fe II $\lambda 5169$ line does not scale with ejecta mass and explosion energy in the way assumed by Popov (1993). Rather, as found observationally by Hamuy (2003) and explained by Kasen & Woosley (2009), agreement in L_{50} entails agreement in velocities measured near the photosphere at day 50 (as we show in Figures 21 and 22).

As our work was being completed, Dessart & Hillier (2019) submitted a paper that also highlights the nonuniqueness of light-curve modeling for varied progenitor masses due to core size and mass loss due to winds. Here we additionally highlight the nonuniqueness of light-curve modeling even for varied ejecta mass. As such, our calculated scaling relationships yield families of explosions with varied R , M_{ej} , and E_{exp} that could produce comparable light curves and similar observed Fe II $\lambda 5169$ line velocities (see, e.g., Figures 25 and 26). Given an independent measurement of the progenitor R , along with a bolometric light curve and an observed nickel mass (M_{Ni}) extracted from the tail, one can directly constrain M_{ej} and E_{exp} . Otherwise, these families of explosions can be used as a starting point to guide further detailed, possibly 3D, modeling for observed events.

2. Our Models

Our modeling takes place in three steps. First, we construct a suite of core-collapse SN progenitor models through the Si-burning phase using MESA following the `example_make_pre_ccsn` test case, described in detail in Paxton et al. 2018 (MESA IV). Second, we load a given progenitor model at core infall, excise the core (as described in Section 6.1 of MESA IV), inject energy and Ni, and evolve the model until it approaches shock breakout. This closely follows the `example_ccsn_IIP` test case. Third, to calculate photospheric evolution and light curves after shock breakout, we use the shock breakout profile produced in the second step as input into the public distribution of STELLA included within MESA, and run until day 175. At the end of the STELLA run, a post-processing script produces data for comparison to observational results (specifically bolometric

light curves and Fe II $\lambda 5169$ line velocities as described in MESA IV).

In order to create a diversity of progenitor characteristics, we chose models with variations in initial mass M_{ZAMS} , core overshooting f_{ov} and $f_{0,\text{ov}}$, convective efficiency α_{MLT} in the hydrogen envelope, wind efficiency η_{wind} , modest surface rotation $\omega/\omega_{\text{crit}}$, and initial metallicity Z . This study concerns itself especially with achieving diversity in the ejecta mass M_{ej} by means of the final mass at the time of explosion M_{final} and the radius R at the time of the explosion. Table 1 lists physical characteristics of all progenitor models utilized in this paper with L_{prog} = the stellar luminosity just prior to explosion. Our naming convention is determined by the ejecta mass and radius at shock breakout, $M \langle M_{\text{ej}} \rangle R \langle R \rangle$. For our sample of SNe IIP models, we use three progenitor models from MESA IV, the 99em_19, 99em_16, and 05cs models, renamed M16.3_R608, M12.9_R766, and M11.3_R541, respectively. Additionally, we create three new models using MESA revision 10398 to capture different regions of parameter space. We created a model with the same input parameters as 99em_19, here named M15.7_R800. In order to explore a diversity of radii for similar parameters, we also created M15.0_R1140, a model with nearly identical input to M15.7_R800, except for reduced efficiency of convective mixing $\alpha_{\text{MLT}} = 2.0$ (the default value is $\alpha_{\text{MLT}} = 3.0$) to create a more radially extended star with otherwise similar properties. Finally, in order to include smaller progenitor radii and mass in our suite, we created M9.3_R433, which has the same progenitor parameters as the 12A-like progenitor model from MESA IV, except greater overshooting $f_{\text{ov}} = 0.01$. These “standard suite” models are denoted by an asterisk in Table 1. All models are solar metallicity, except the 05cs-like progenitor from MESA IV, M11.3_R541, which has metallicity $Z = 0.006$.

Beyond this standard suite, we construct M20.8_R969, an $M_{\text{ZAMS}} = 25 M_{\odot}$ nonrotating model with no overshooting and wind efficiency $\eta_{\text{wind}} = 0.4$, which has a very tightly bound core and leads to significant fallback at energies $E_{\text{exp}} < 2 \times 10^{51}$ erg (see also Appendix A). Additionally, to highlight the families of explosions that produce comparable light curves (see Section 7), we construct three progenitor models that, when exploded with the proper explosion energy, all produce light curves similar to that of our M12.9_R766 model exploded with 0.6×10^{51} erg and $M_{\text{Ni}} = 0.045 M_{\odot}$. M9.8_R909 was $M_{\text{ZAMS}} = 13.7 M_{\odot}$ with a final mass of

11.4 M_{\odot} , created with overshooting $f_{\text{ov}} = 0.016$, $f_{0,\text{ov}} = 0.006$, initial rotation $(v/v_c)_{\text{ZAMS}} = 0.2$, wind efficiency $\eta_{\text{wind}} = 1.0$, and $\alpha_{\text{MLT}} = 2.0$. M10.2_R848 was $M_{\text{ZAMS}} = 13.5 M_{\odot}$ with a final mass of $12.0 M_{\odot}$, which was created with overshooting $f_{\text{ov}} = 0.01$, $f_{0,\text{ov}} = 0.004$, initial rotation $(v/v_c)_{\text{ZAMS}} = 0.2$, wind efficiency $\eta_{\text{wind}} = 0.8$, and $\alpha_{\text{MLT}} = 2.0$. M17.8_R587 was $M_{\text{ZAMS}} = 20.0 M_{\odot}$ with a final mass of $19.41 M_{\odot}$, which was created with no overshooting, no rotation, wind efficiency $\eta_{\text{wind}} = 0.2$, and $\alpha_{\text{MLT}} = 3.5$.

During the explosion phase, which we carry out using MESA revision 10925 to include an updated treatment of fallback (see Appendix A), we vary the total energy of the stellar model at the time of explosion (E_{tot}) from 2×10^{50} erg to 2×10^{51} erg, with 0.2, 0.3, 0.4, 0.5, 0.6, 0.7, 0.8, 1.0, 1.2, 1.4, 1.6, and 2.0 $\times 10^{51}$ erg. These models are significantly impacted by the Duffell (2016) prescription for mixing via the Rayleigh–Taylor instability, which smooths out the density profile and leads to the mixing of H deep into the interior of the ejecta and ^{56}Ni out toward the outer ejecta (see MESA IV). We use the RTI coefficient $D_{\mathcal{R}} = 3.0$. For a further exploration of the impact of changing the strength of RTI-driven mixing on ejecta and light-curve evolution, see the work of P. Duffell et al. (2019, in preparation).

At the handoff between MESA and STELLA, we initialize STELLA with 400 zones and 40 frequency bins, and an error tolerance 0.001 for the Gear–Brayton method (Gear 1971; Brayton et al. 1972), which leads to converged models. We also rescale the abundance profile of ^{56}Ni and ^{56}Co to match a specified total nickel mass M_{Ni} . This resets the nickel decay clock to the time of shock breakout. We consider ^{56}Ni masses of $M_{\text{Ni}}/M_{\odot} = 0.0, 0.015, 0.03, 0.045, 0.06, \text{ and } 0.075$; the impact of ^{56}Ni in our models is discussed in detail in Section 5. As most of the mixing is accounted for by Duffell RTI, we only employ modest boxcar smoothing of abundance profiles at handoff as recommended in MESA IV, using three boxcar passes with a width of $0.8 M_{\odot}$. Additionally, as described in Paxton et al. 2019 and Appendix A here, we use a minimum innermost velocity cut of material moving slower than 500 km s^{-1} to prevent numerical artifacts in STELLA caused during interactions between reverse shocks and slow-moving material near STELLA’s inner boundary (IB). This study concerns itself with intrinsic properties of the SNe and their progenitors, determined primarily by quantities on the plateau, and therefore we do not include circumstellar material (CSM) in STELLA.

2.1. Estimating Fallback

Even when the total energy of a stellar model is greater than zero (i.e., the star is unbound), it is possible for some of the mass that does not collapse into the initial remnant object to become bound and fall back onto the central object, which we define as M_{fallback} . This typically occurs as a result of inward-propagating shock waves generated at compositional boundaries within the ejecta. The relationship between progenitor binding energy, explosion energy, and fallback can be seen in Figure 1, which shows the final mass of our models versus the total energy deposited E_{dep} , which is equal to the total energy of the model after the explosion E_{tot} plus the magnitude of the total energy of the bound progenitor model at the time of explosion E_{bind} . Fallback is particularly common in explosions where the explosion energy is not significantly larger than the binding energy of the model at the time of explosion. In

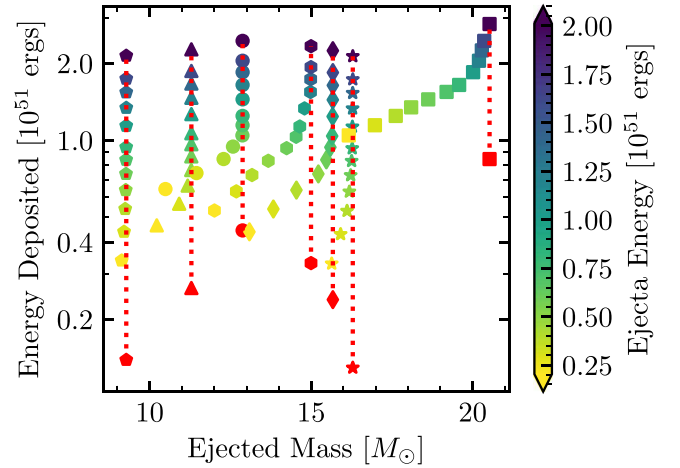


Figure 1. Energy deposited in the explosion vs. ejected mass for our standard suite, as well as for the M20.8_R969 model, all exploded at 12 different explosion energies. Marker shapes correspond to different initial progenitor models as follows: pentagon—M9.3_R433; triangle—M11.3_R541; circle—M12.9_R766; hexagon—M15.0_R1140; diamond—M15.7_R800; star—M16.3_R608; square—M20.8_R969. Explosions that would have $E_{\text{tot}} = 0$ (corresponding to $E_{\text{dep}} = |E_{\text{bind}}|$) are shown as red symbols whose x-coordinate is determined by the same model assuming no fallback. The red dotted lines serve as a visual guide, indicating explosions with no fallback for each progenitor model. Color corresponds to the total energy of the ejecta just after the explosion E_{tot} .

general, more tightly bound models require larger total final energies to unbind the entirety of the potential ejecta.

The proper treatment of fallback in 1D simulations remains an open question because of complexities such as the interaction between accretion-powered luminosity and the IB of the explosion models. In MESA, the current implementation of fallback is effective as a computationally robust approximation that allows experimentation, but it should not be viewed as an accurate model of the physical processes at work. Consequently, we restrict our study to models with little fallback material: $M_{\text{fallback}} < 0.4 M_{\odot}$. The models that survive this cut are shown in Figure 2. For a full description of our treatment of fallback, see Appendix A.

3. Analytic Expectations

The luminosity of an SN IIP is, approximately, powered by shock cooling due to expansion out to around 20 days (the “shock cooling phase”), then hydrogen recombination until around 100 days (the “plateau phase”), and the radioactive decay chain of $^{56}\text{Ni} \rightarrow ^{56}\text{Co} \rightarrow ^{56}\text{Fe}$ beyond that (the “nickel tail”). The expansion time of the SN ejecta is expressed as $t_e \approx R/v_{\text{SN}}$, where R is the radius of the star at the time of the explosion, and the velocity v_{SN} is defined by the mass of the ejecta M_{ej} and kinetic energy of the ejecta at infinity $E_{\text{exp}} = M_{\text{ej}} v_{\text{SN}}^2/2$.⁴ Similarly, the time it takes to reach shock breakout after core collapse (t_{SB}) scales with t_e , such that

$$t_{\text{SB}} \approx 0.91 \text{ days } R_{500} E_{51}^{-1/2} M_{10}^{1/2}, \quad (1)$$

where $R_{500} = R/500 R_{\odot}$, $E_{51} = E_{\text{exp}}/10^{51} \text{ erg}$, and $M_{10} = M_{\text{ej}}/10 M_{\odot}$, and the dimensionful prefactor comes from a linear fit to our numerical models. This timescale is primarily a

⁴ During the homologous phase, the kinetic energy of the ejecta is approximately equivalent to the total energy of the explosion, since radiation accounts only for a small fraction of the total energy at late times.

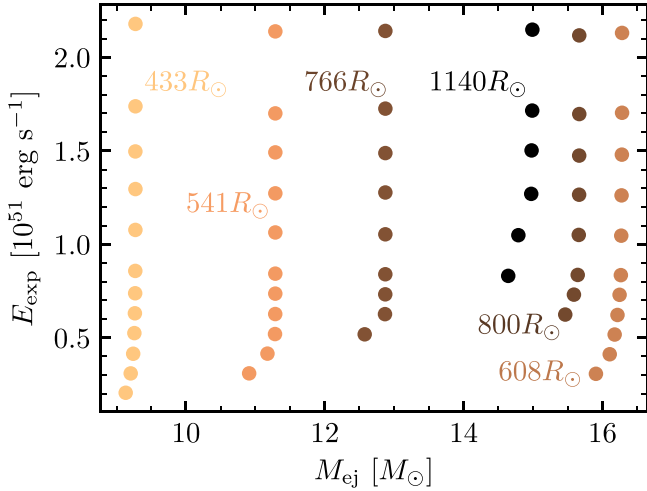


Figure 2. Ejecta masses and explosion energies as determined by the kinetic energy at day 50 in STELLA considered as a part of our standard suite, with fallback masses $M_{\text{fallback}} < 0.4 M_{\odot}$. Lighter colors correspond to smaller progenitor radii, which are labeled.

property of the models but would observationally correspond to the difference in time between the first neutrino signal from core collapse and the first detection in the electromagnetic spectrum from shock breakout.

Following Kasen & Woosley (2009), in the limit of no accumulated heating of the ejecta due to ^{56}Ni decay, the luminosity on the plateau (taken here to be at day 50, denoted L_{50}) is set by the total internal energy (E) to be radiated out divided by the duration of the plateau:

$$L_{50} = \frac{E(t_p)}{t_p} = \frac{E_0 t_e}{t_p^2}, \quad (2)$$

where t_p is the duration of the plateau, $E_0 \approx E_{\text{exp}}/2$ is the initial internal energy of the ejecta at shock breakout, and the second equality comes from assuming the internal energy evolution for homologous expansion (where $r(t) \approx vt$, for a Lagrangian fluid element with constant velocity v) in a radiation-dominated plasma, $E_0 t_e = E(t_p) t_p$.

Here we compare to the analytics of Popov (1993), which consider the effects of both H recombination and radiative diffusion. Historically, analytic scalings that ignore recombination (Arnett 1980) or radiative diffusion (Woosley & Weaver 1988; Chugai 1991) have also been considered. These scalings are also detailed in Kasen & Woosley (2009) and Sukhbold et al. (2016). From a two-zone model including an optically thick region of expanding ejecta behind the photosphere and an optically thin region outside the photosphere, Popov finds that the luminosity on the plateau (here taken at day 50) and duration of the plateau should scale as

$$\begin{aligned} L_{50} &\propto M^{-1/2} E_{\text{exp}}^{5/6} R^{2/3} \kappa^{-1/3} T_1^{4/3}, \\ t_0 &\propto M^{1/2} E_{\text{exp}}^{-1/6} R^{1/6} \kappa^{1/6} T_1^{-2/3}, \end{aligned} \quad (3)$$

where κ is the opacity in the optically thick component of the ejecta, T_1 is the ionization temperature of hydrogen, and M is the relevant mass (which could depend on the extent to which H is mixed throughout the ejecta). Kasen & Woosley (2009)

recover a similar set of scalings from their models:

$$\begin{aligned} L_{50} &\propto M_{\text{ej}}^{-1/2} E_{\text{exp}}^{5/6} R^{2/3} X_{\text{He}}^1, \\ t_0 &\propto M_{\text{ej}}^{1/2} E_{\text{exp}}^{-1/4} R^{1/6} X_{\text{He}}^{1/2}, \end{aligned} \quad (4)$$

where X_{He} is the mass fraction of He. There is some disagreement in the literature as to whether the mass M used in the Popov scalings should be the mass of the hydrogen-rich envelope (M_{env}) or the mass of the ejecta (M_{ej}). Sukhbold et al. (2016), for example, use M_{env} in recreating these scalings, since recombination in the hydrogen-rich envelope drives the evolution of the SN, with little contribution from the hydrogen-poor innermost ejecta coming from the core. However, in our models, the relevant mass is the *total* ejecta mass M_{ej} , as we see mixing of hydrogen deep into the interior of the star and core elements into the envelope due to RTI. Since hydrogen recombination thus plays a significant role in setting the temperature throughout the entirety of the ejecta, it is the entire ejecta mass that is used in the scalings we derive later. Additionally, we make the assumption that by day 50, E_{exp} is equal to the kinetic energy of the ejecta.

Popov also recommended assuming that the observed photospheric velocity of the SN ejecta should scale like v_{SN} , such that $v_{\text{ph}} \propto (E_{\text{exp}}/M_{\text{ej}})^{1/2}$. However, this scaling, which does describe the *typical* velocity of the SN ejecta, should not be used when describing photospheric velocities at a fixed time, for reasons we discuss in Section 6.

The above scalings do not take into account additional heating by the radioactive decay chain of ^{56}Ni , which does not significantly affect the luminosity on the plateau, but does extend the duration of the plateau by heating the ejecta at late times. We discuss more detailed expectations for the effects of ^{56}Ni in Appendix B and its impact on our models in Section 5. This correction is typically written as

$$t_p = t_0 \times f_{\text{rad}}^{1/6}, \quad (5)$$

where f_{rad} can be expressed as

$$f_{\text{rad}} = 1 + C_f M_{\text{Ni}} M_{\text{ej}}^{-1/2} E_{\text{exp}}^{-1/2} R^{-1}, \quad (6)$$

and C_f is a numerical prefactor that encodes the energy and decay time of the ^{56}Ni decay chain (Kasen & Woosley 2009; Sukhbold et al. 2016; and Appendix B).

These scaling relationships serve as a useful guide when modeling SN IIP light curves. However, complexities arising from changes in temperature profiles, density profiles, realistic distributions of important elements such as H and ^{56}Ni , and stellar structure can lead to differences between these simple analytic expectations and numerical models. For example, the Popov analytics are derived for emission from a two-zone model with an optically thick inner region with a single opacity κ and an optically thin outer region with a flat density profile. More realistic evolution of the temperature and density profiles of one of our SN ejecta models is shown in Figure 3, akin to Figure 11 of Urobin (2007).

Thus, in the following sections we aim to provide expressions that relate observables to the physical properties of the explosions, namely, the progenitor R , M_{ej} , and E_{exp} , while also capturing the ejecta structure underlying these events.

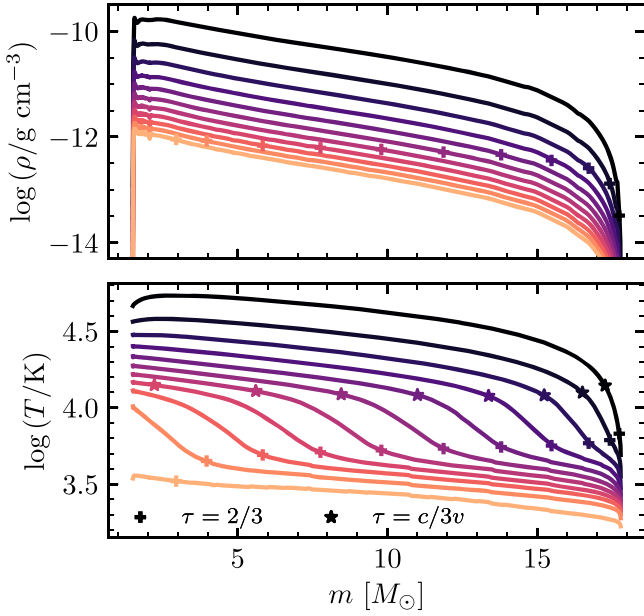


Figure 3. Density (top panel) and temperature (bottom panel) of the ejecta at every 10 days in the evolution starting at day 20 for our M16.3_R608 model exploded with 10^{51} erg and $M_{\text{Ni}} = 0.03M_{\odot}$. Darker colors indicate earlier times. Also plotted are the photosphere ($\tau = 2/3$; plus signs) and the location where $\tau = c/3v$ (stars), which is shown only on the temperature plot to reduce clutter, to demonstrate the extent of the region where the photon diffusion time is shorter than the expansion time.

4. Luminosity at Day 50

We use the bolometric luminosity 50 days after shock breakout, L_{50} , as our diagnostic for the plateau luminosity, as in most cases this is beyond the time where shock heating of CSM would affect the luminosity (Morozova et al. 2017). Moreover, for all but one progenitor model, increasing the amount of ^{56}Ni has a negligible impact on L_{50} , as the internal energy at day 50 of the outer region of the ejecta is still dominated by the initial shock. However, in explosions where the plateau is naturally short, there can be marginal, but noticeable, additional luminosity at day 50 from ^{56}Ni decay. This can be seen in Figure 4, which shows the differences between a selection of light curves and the corresponding light curves with no ^{56}Ni . We show light curves for M16.3_R608, a typical model with a typical $M_{\text{Ni}} = 0.03M_{\odot}$ (left), and for high $M_{\text{Ni}} = 0.075M_{\odot}$ explosions of the only progenitor model in which we see significant deviation in L_{50} as a result of ^{56}Ni heating, M9.3_R433 (right), where L_{50} varies by up to 15% between an explosion with no ^{56}Ni and one with $M_{\text{Ni}} = 0.075M_{\odot}$. Noting this, we choose a moderate, constant value of $M_{\text{Ni}} = 0.03M_{\odot}$, typical of observed events (Müller et al. 2017), and calculate how L_{50} scales with M_{ej} , E_{exp} , and R .

We fit two formulae to our sample suite of 57 explosions. First, we assume the power-law coefficients of Popov (1993) and let the normalization float, finding

$$\begin{aligned} \log(L_{50}/[\text{erg s}^{-1}]) \\ = 42.18 - \frac{1}{2}\log M_{10} + \frac{5}{6}\log E_{51} + \frac{2}{3}\log R_{500}, \end{aligned} \quad (7)$$

where 42.18 is a linear fit from our models and logarithms are base 10, with $M_{10} = M_{\text{ej}}/10M_{\odot}$, $R_{500} = R/500R_{\odot}$, and $E_{51} = E_{\text{exp}}/10^{51}$ erg. For these models, rms deviations of L_{50} from values derived by applying Equation (7), corresponding to

the blue circles in Figure 5, are 7.9%, with a maximum deviation in L_{50} of 32%. The normalization for an explosion with $M_{10} = R_{500} = E_{51} = 1$ is comparable to but somewhat lower than the value of 42.27 given in Sukhbold et al. (2016) (who use M_{env} rather than M_{ej}), as well as the value of 42.21 calculated in Popov (1993) for default H recombination temperatures and opacities. Kasen & Woosley (2009) give a value of $42.10 + \log(X_{\text{He}}/0.33)$, letting X_{He} range from 0.33 to 0.54.

We perform a second fit for the normalization *and* the power laws in M_{10} , E_{51} , and R_{500} , and we recover scalings that are similar to those in Equation (7). We find a slightly shallower scaling with M_{ej} and E_{exp} and a slightly steeper dependence on R_{500} :

$$\begin{aligned} \log(L_{50}/[\text{erg s}^{-1}]) \\ = 42.16 - 0.40\log M_{10} + 0.74\log E_{51} + 0.76\log R_{500}, \end{aligned} \quad (8)$$

where the normalization and power-law coefficients are fit from our models. The rms deviation of the models from Equation (8), shown as red triangles in Figure 5, is 4.7%, with deviations not exceeding 14.3% for any model with $M_{\text{Ni}} = 0.03M_{\odot}$. This is a better fit than the one that assumes the exact Popov scaling.

The luminosities of our models, as they compare to the fitted formulae, are shown in Figure 5. Most models agree with the Popov scaling, while the Popov scaling overpredicts L_{50} in low ejecta mass, high explosion energy cases. The x -axis of Figure 5 is t_{SB} , chosen because it scales with explosion energy for a fixed ejecta mass and radius (Equation (1)) and increases with increasing M_{ej} and R , visually distinguishing the six different progenitor models and different explosion energies.

Although the presence of ^{56}Ni does not affect light-curve properties at day 50 in a majority of models, in a few explosions there is slight variation in L_{50} introduced by the extra heating from ^{56}Ni (seen in Figure 4). Because this effect is only distinctly noticeable in our model with the smallest values of M_{ej} and R , this can lead to variations in our recovered power laws when fitting to different fixed ^{56}Ni masses. However, this correction is typically small, falling within the scatter in which our models agree with the fitted formulae. We find that the power-law scalings of Equation (8) describe all models with M_{Ni} ranging from 0.0 to $0.075M_{\odot}$ within 18.2%, with rms deviations of 4.8%, where the largest deviations occur in events where $M_{\text{Ni}} = 0.0M_{\odot}$, which are not consistent with any observed SNe IIP.

We now use Equation (8) to compare our MESA+STELLA results to models from other software instruments. In Table 2, we show our predictions for L_{50} compared against luminosities from the MESA+CMFGEN models (without Duffell RTI) of Dessart et al. (2013), the Kepler+Sedona models of Kasen & Woosley (2009), and the MESA+CMFGEN models in Lisakov et al. (2017). In general, the disagreement between our formula and these other models is similar to the scatter within our own models, with the exception of the two lowest-energy explosions in Kasen & Woosley (2009) and the low-luminosity suite in Lisakov et al. (2017). Equation (8) agrees with the Dessart et al. (2013) models, with an rms error of 9%, but slightly underpredicts luminosity in a majority of cases. Compared to the models of Kasen & Woosley (2009), Equation (8) gives rms errors of 17% with no clear under- or

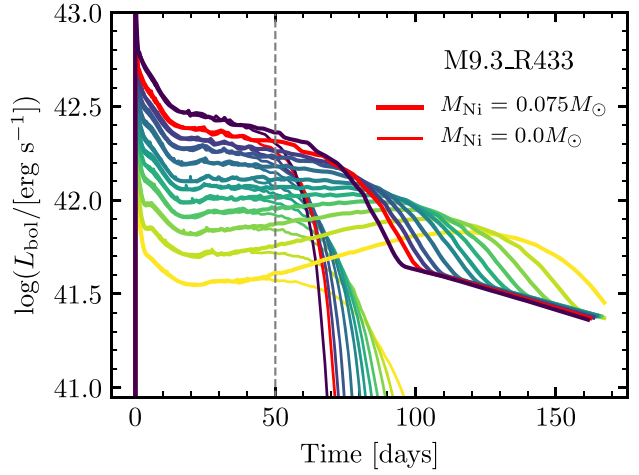
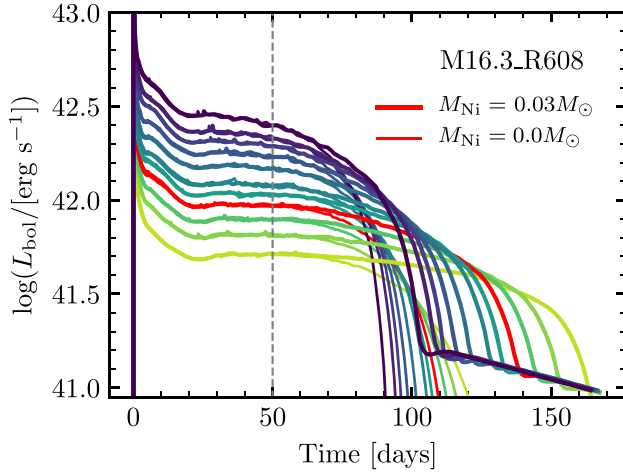


Figure 4. Light curves for increasing explosion energies of our M16.3_R608 model with $M_{\text{Ni}} = 0.03 M_{\odot}$ (left) and our smallest model, M9.3_R433, with $M_{\text{Ni}} = 0.075 M_{\odot}$ (right). Thin lines correspond to the same explosions, but with no ^{56}Ni . The red lines correspond to the models with the typical M_{Ni} given L_{50} , from the relationship in Pejcha & Prieto (2015b), and their no-nickel counterparts.

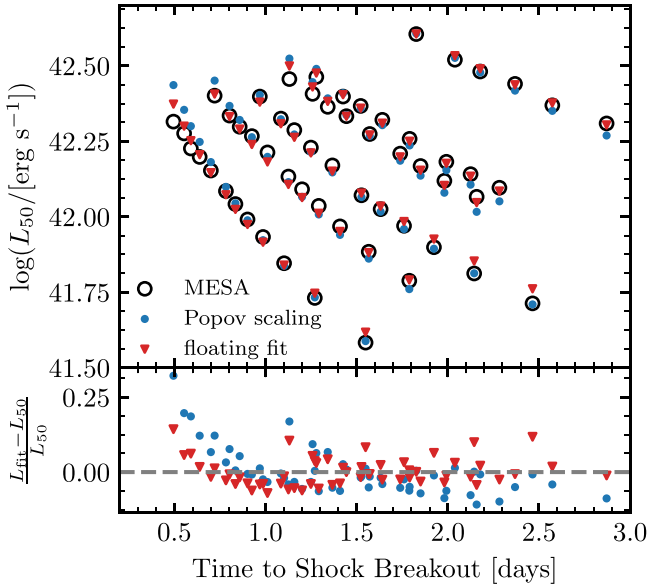


Figure 5. Fitting formula predictions for L_{50} (colored markers) compared with the model L_{50} (black circles; top panel), and their residuals (bottom panel) for our suite of 57 explosions at constant $M_{\text{Ni}} = 0.03 M_{\odot}$. Each diagonal family of points reflects one progenitor model exploded with different energies.

overprediction. The low-luminosity models from Lisakov et al. (2017) have greater disagreement, with rms errors of 23% from Equation (8). This is not surprising, as on the low-luminosity end our treatment of fallback discussed in Section 2 and Appendix A excludes most models in this region of parameter space from our fitting formulae, as significant fallback after the initial core collapse is often seen for low explosion energies.

5. Plateau Duration and ET

Although the plateau duration t_p is theoretically motivated by Popov (1993), Kasen & Woosley (2009), and others, it is important to reliably extract it from our models as well as observations. We discuss two ways of extracting t_p , one defined by observables and the other extracted from properties of the

theoretical models, which we use to evaluate the impact of ^{56}Ni .

For a definition that can be applied to observed or calculated light curves, we follow Valenti et al. (2016), fitting the following functional form to the logarithm, $y(t)$, of the bolometric luminosity around the fall from the plateau:

$$y(t) = \log_{10}(L_{\text{bol}}) = \frac{-A_0}{1 + e^{(t-t_p)/W_0}} + (P_0 \times t) + M_0. \quad (9)$$

An example is shown in Figure 6. We use the python routine `scipy.optimize.curve_fit` to fit the light curve starting at the time when the luminosity evolution is 75% of the way to its steepest descent, defined when $d \log L_{\text{bol}}/dt$ is at its most negative after the initial drop at shock breakout, which occurs shortly before transitioning to the nickel tail. We fix the value of P_0 to be the slope on the ^{56}Ni tail. We interpret the fitting parameter t_p to be the plateau duration.

As the recombination-powered photosphere moves into the innermost ejecta, the optical depth at the IB declines by orders of magnitude and the photospheric temperature plummets. This transition, shown in Figure 7, is the physical end of the plateau. Thus, for our modeling definition of the plateau duration, we use the time, after shock breakout, when the optical depth τ_{IB} through the ejecta becomes < 10 . This time will be denoted hereafter as $t_{\tau=10}$ and can be used as a metric for plateau duration when comparing to models where there is no ^{56}Ni , where Equation (9) does not accurately capture the fall from the plateau. As shown by the black markers in Figure 7, the observable t_p roughly corresponds to the physical end of the plateau phase around $t_{\tau=10}$. Across all progenitor models, explosion energies, and nonzero nickel masses that we consider, rms differences between $t_{\tau=10}$ and t_p are 4.1%, and all differences are within $\pm 7\%$.

5.1. Impact of ^{56}Ni on Plateau Duration in Our Models

The presence of radioactive ^{56}Ni prolongs the photospheric evolution and extends the plateau by providing extra heat to the ejecta. This is shown in Figure 8, where we show ejecta temperature profiles of the same SN explosion with different

Table 2

Comparison of Equation (8) to CMFGEN Models from Dessart et al. (2013), Kepler+Sedona Models from Kasen & Woosley (2009), and Low-luminosity CMFGEN Models from Lisakov et al. (2017)

Source	Model	M_{ej} (M_{\odot})	E_{exp} (10^{51} erg)	R (R_{\odot})	L_{50} (10^{42} erg s $^{-1}$)	Equation (8) (10^{42} erg s $^{-1}$)	Percent Diff. (%)
Dessart+13	m15Mdot	10.01	1.28	776	2.55	2.40	−5
	m15	12.48	1.27	768	2.56	2.17	−15
	m15e0p6	12.46	0.63	768	1.19	1.29	8
	m15mlt1	12.57	1.24	1107	3.13	2.81	−10
	m15mlt3	12.52	1.34	501	1.61	1.63	1
	m15os	10.28	1.40	984	3.49	3.05	−12
	m15r1	11.73	1.35	815	2.62	2.44	−7
	m15r2	10.39	1.34	953	3.30	2.87	−13
	m15z2m3	13.29	1.35	524	1.70	1.65	−3
	m15z4m2	11.12	1.24	804	2.48	2.31	−6
	s15N	10.93	1.20	810	2.51	2.29	−9
	s150	13.93	1.20	610	2.47	2.29	−8
K&W 2009	M12_E1.2_Z1	9.53	1.21	625	1.91	1.99	4
	M12_E2.4_Z1	9.53	2.42	625	3.67	3.33	−9
	M15_E1.2_Z1	11.29	1.21	812	2.16	2.27	5
	M15_E2.4_Z1	11.29	2.42	812	4.35	3.80	−12
	M15_E0.6_Z1	11.25	0.66	812	1.26	1.45	15
	M15_E4.8_Z1	10.78	4.95	812	7.80	6.59	−15
	M15_E0.3_Z1	11.27	0.33	812	0.59	0.87	46
	M20_E1.2_Z1	14.36	1.22	1044	2.61	2.52	−4
	M20_E2.4_Z1	14.37	2.42	1044	4.85	4.18	−13
	M20_E0.6_Z1	14.36	0.68	1044	1.40	1.63	17
	M20_E4.8_Z1	14.37	4.99	1044	8.57	7.16	−17
	M25_E1.2_Z0.1	13.27	1.26	632	1.67	1.82	8
	M25_E2.4_Z0.1	13.24	2.48	632	3.08	3.00	−2
	M25_E0.6_Z0.1	13.28	0.65	632	0.86	1.11	29
	M25_E4.8_Z0.1	13.18	4.90	632	5.31	4.98	−6
Lisakov+17	X	8.29	0.25	502	0.446	0.550	24
	XR1	8.08	0.26	581	0.513	0.643	23
	XR2	7.90	0.27	661	0.592	0.737	24
	XM	9.26	0.27	510	0.423	0.567	34
	YN1	9.45	0.25	405	0.381	0.446	17
	YN2	9.45	0.25	405	0.381	0.446	17
	YN3	9.45	0.25	405	0.375	0.446	19

Note. Bolometric luminosities at day 50 for Dessart et al. (2013) are recovered from light curves provided by L. Dessart (2017, private communication). These luminosities are compared to Equation (8) applied to M_{ej} , E_{exp} , and R from the various models.

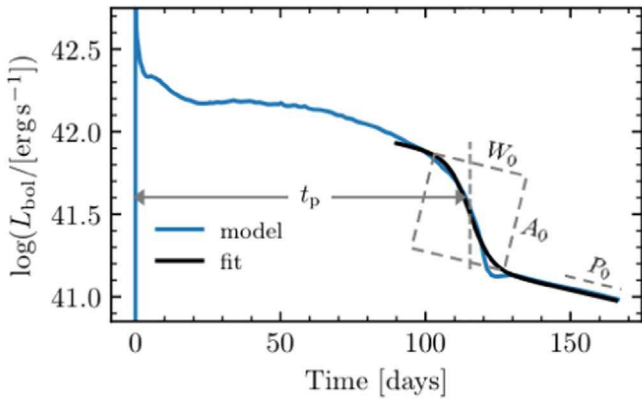


Figure 6. Diagram of fitting Equation (9) to find the 115-day duration of the plateau for our model M16.3_R608 exploded with $E_{\text{exp}} = 10^{51}$ erg and $M_{\text{Ni}} = 0.03M_{\odot}$. Fitting parameters are labeled, but we only ascribe physical significance to t_p .

M_{Ni} . At day 50, the photosphere for all models remains in the outer ejecta, where there is very little ^{56}Ni . At later times, the photosphere has moved in farther for models with lower M_{Ni} ,

whereas additional heat from the ^{56}Ni decay chain causes the recombination-powered photosphere to move in more slowly in models with higher M_{Ni} .

The analytics in Appendix B and Section 3 treat the ejecta as a single zone, with heating from ^{56}Ni decay throughout. However, ^{56}Ni is more highly concentrated in the center of the ejecta. Thus, heat from ^{56}Ni decay remains trapped in the optically thick inner region, extending the plateau more at late times. This more concentrated ^{56}Ni heating should have a more significant impact on the plateau duration than it would for an analytic one-zone model, as the internal energy of the inner ejecta is more relevant than that of the ejecta as a whole at the end of the plateau. Figure 9 shows the diversity of asymptotic ^{56}Ni and hydrogen distributions within our standard suite of models at handoff to STELLA for the highest-energy ($E_{\text{tot}} = 2 \times 10^{51}$ erg), highest nickel mass ($M_{\text{Ni}} = 0.075M_{\odot}$) cases.

Moreover, the distribution of ^{56}Ni , which can vary among different progenitors depending on core structure and mixing, can also introduce inherent scatter to the plateau duration (Kozyreva et al. 2018). Figure 10 shows light curves and ^{56}Ni profiles for

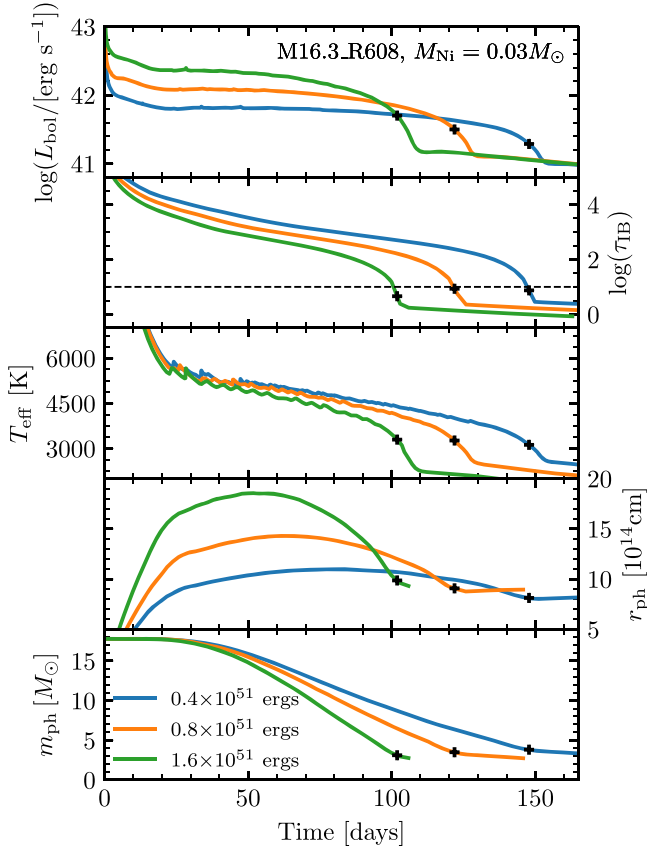


Figure 7. Evolution of luminosity, optical depth at the IB (τ_{IB}), effective temperature (T_{eff}), photospheric radius (r_{ph}), and mass coordinate of the photosphere (m_{ph}) for our M16.3_R608 model, exploded with $M_{\text{Ni}} = 0.03M_{\odot}$ at three different explosion energies, showing the transition to the end of the plateau. Black plus signs indicate the end of the plateau determined from fitting Equation (9). The thin dashed line in the second panel indicates $\tau_{\text{IB}} = 10$.

the M16.3_R608 model exploded with $E_{\text{exp}} = 10^{51}$ erg and $M_{\text{Ni}} = 0.03M_{\odot}$, where the same ^{56}Ni mass is redistributed by hand at the time of shock breakout out to some fraction of the ejecta. Although this exercise spans a greater diversity in ^{56}Ni concentration than any of our models, we see for this otherwise unexceptional light curve that the plateau duration t_{p} can vary by almost 10 days.

A full examination of the effects of changing the distributions in the framework of the Duffell RTI prescription (Paxton et al. 2018) is beyond the scope of this paper and will be the subject of future study (P. Duffell et al. 2019, in preparation). Here we examine the impact of ^{56}Ni on the value of f_{rad} in $t_{\text{p}} = t_0 \times f_{\text{rad}}^{1/6}$ (Equation (5)), where t_0 is the plateau duration for the same explosion with no ^{56}Ni .

Following Kasen & Woosley (2009), Sukhbold et al. (2016), and others, ^{56}Ni extends the plateau as

$$t_{\text{p}}/t_0 = (1 + C_f M_{\text{Ni}} E_{51}^{-1/2} M_{10}^{-1/2} R_{500}^{-1})^{1/6}, \quad (10)$$

and we can extract C_f by fitting to our models using the $t_{\tau=10}$ definition of plateau duration. We consider all six progenitor models with explosion energies sufficient to cause minimal fallback, with $M_{\text{Ni}}/M_{\odot} = 0.0, 0.015, 0.03, 0.045, 0.06$, and 0.075 . We exclude models where the plateau is so long that the nickel tail does not appear at any point in our simulations, as well as models that have less than half a decade drop in L_{bol}

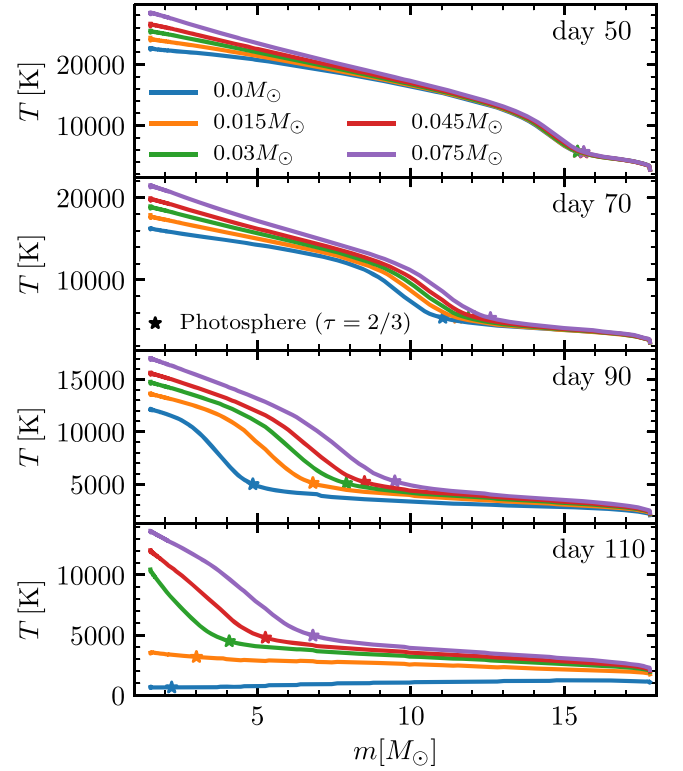


Figure 8. Ejecta temperature profiles at different times with increasing amounts of ^{56}Ni for our M16.3_R608 model exploded with 10^{51} erg. The location of the photosphere is shown for each model by the colored stars.

from day 50 to the top of the nickel tail, as no such events have been observed.⁵

This gives a total of 332 light curves, including the 57 with no ^{56}Ni , which we compare to the light curves of identical explosions with no ^{56}Ni . Figure 11 shows the ratio of the plateau duration, $t_{\tau=10}$, of each of these light curves compared to $t_{\tau=10}$ for an identical explosion with no ^{56}Ni , t_0 , following Kasen & Woosley (2009) but with our suite of 332 model light curves. We recover $C_f \approx 87$, which is an order of magnitude larger than the approximate lower bound $C_f \approx 7.0$ derived in Appendix B, and roughly a factor of 4 larger than $C_f = 24$ (derived in Kasen & Woosley 2009, typographical error corrected in Sukhbold et al. 2016). This likely results from the different ^{56}Ni mass distributions in our models from those in Kasen & Woosley (2009). As demonstrated in Figure 10, this can yield significant differences in the plateau duration. Our fit shows similar scatter for all ^{56}Ni masses considered, with more scatter introduced by intrinsic differences among the individual models than by the changing M_{Ni} . For $M_{\text{Ni}} \gtrsim 0.03M_{\odot}$, this typically leads to a 20%–60% increase in the plateau duration.

5.2. Plateau Durations for Nickel-rich Events

For nickel-rich events, the ^{56}Ni and ^{56}Co decay dominates the internal energy of the inner ejecta, such that

⁵ This primarily excludes models at high nickel masses and low explosion energies, specifically M9.3_R433 ($E_{51} = 0.2$ with $M_{\text{Ni}} = 0.075M_{\odot}$), M11.3_R541 ($E_{51} = 0.3$ with $M_{\text{Ni}} = 0.06M_{\odot}$ and $M_{\text{Ni}} = 0.075M_{\odot}$), and M16.3_R608 ($E_{51} = 0.3$ with $M_{\text{Ni}} = 0.045M_{\odot}$, $M_{\text{Ni}} = 0.06M_{\odot}$, and $M_{\text{Ni}} = 0.075M_{\odot}$; $E_{51} = 0.4$ with $M_{\text{Ni}} = 0.06M_{\odot}$ and $M_{\text{Ni}} = 0.075M_{\odot}$; and $E_{51} = 0.4$ with $M_{\text{Ni}} = 0.075M_{\odot}$).

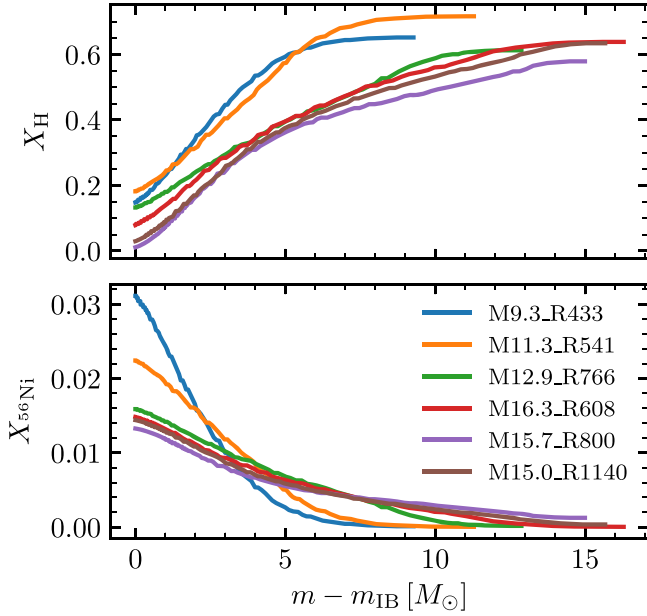


Figure 9. Diversity of H (top panel) and ^{56}Ni (bottom panel) profiles for our standard suite of models, exploded with our highest E_{exp} and M_{Ni} . The x-axis is the mass coordinate within the ejecta.

$C_f M_{\text{Ni}} M_{10}^{-1/2} E_{51}^{-1/2} R^{-1} > 1$. Assuming that t_0 scales as in Popov (1993), we can approximate

$$\begin{aligned} t_p &\propto M_{\text{ej}}^{1/2} E_{\text{exp}}^{-1/6} R^{1/6} \times (1 + C_f M_{\text{Ni}} M_{\text{ej}}^{-1/2} E_{\text{exp}}^{-1/2} R^{-1})^{1/6} \\ &\rightarrow t_p \propto M_{\text{Ni}}^{1/6} M_{\text{ej}}^{5/12} E_{\text{exp}}^{-1/4}. \end{aligned} \quad (11)$$

The two features of interest are the power-law behavior and the disappearing scaling with the progenitor radius. We thus expect that the plateau duration for ^{56}Ni -rich events does not depend on the progenitor radius. To check, we perform a power-law fit for t_p as a function of M_{Ni} , M_{ej} , E_{exp} , and R for 218 model light curves where $M_{\text{Ni}} \gtrsim 0.03 M_{\odot}$. We find that $\log(t_p/\text{days}) = 2.184 + 0.134 \log(M_{\text{Ni}}) + 0.429 \log(M_{10})$

$- 0.280 \log(E_{51}) - 0.018 \log(R_{500})$ with rms deviations of 2.10% and a maximum deviation of 8.1%. Since the dynamic range in R is a factor of two and the scaling is negligible, we perform a fit for these same models to only M_{Ni} , M_{ej} , and E_{exp} , recovering

$$\begin{aligned} \log(t_p/\text{days}) &= 2.184 + 0.134 \log(M_{\text{Ni}}) \\ &\quad + 0.411 \log(M_{10}) - 0.282 \log(E_{51}). \end{aligned} \quad (12)$$

These coefficients are excellent matches to the power laws in Equation (11). Our models, as well as their agreement with this fit, are shown in Figure 12. The rms deviations between this fit and our models are 2.13%, with maximum deviation of 7.5%. Typical differences between the plateau durations recovered from the fit and those extracted from our models are 2–5 days, with the largest discrepancy being 11 days, which is for a relatively low-luminosity SN with a plateau duration of 156 days. For all of the scaling equations of this section, the scatter in our models does not require that we report the fits to three decimal places; this is done for the sake of completeness.

We also checked the agreement of Equation (12) with the publicly available light curves from Dessart et al. (2013). For

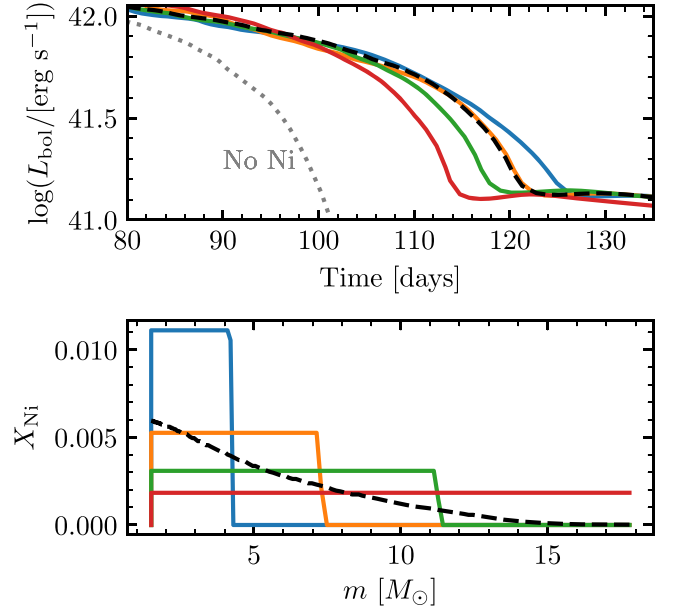


Figure 10. Light curves at the end of the plateau (top panel) and ^{56}Ni distributions (bottom panel) for the M16.3_R608 model exploded with $E_{\text{exp}} = 10^{51}$ erg and $M_{\text{Ni}} = 0.03 M_{\odot}$, for the fiducial explosion (black dashed line), compared to models where ^{56}Ni is redistributed by hand out to some fraction of the ejecta at the time of shock breakout (solid colored lines). The light curve for the same explosion with no Ni is given by the gray dashed line in the top panel.

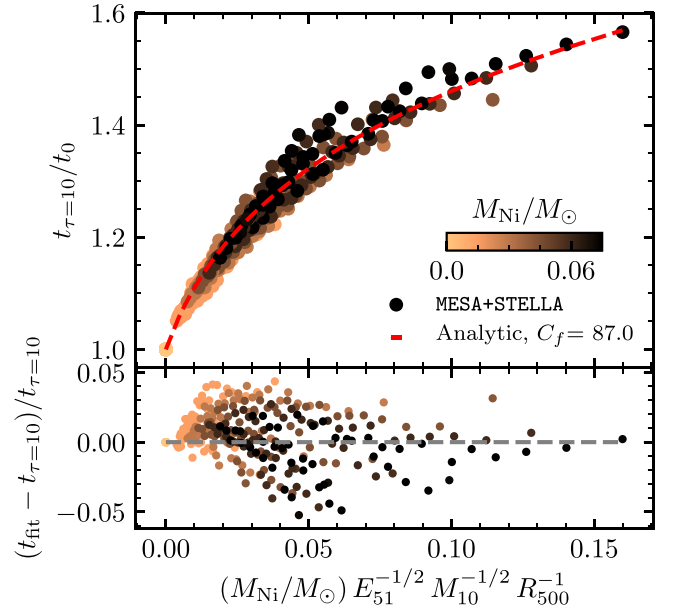


Figure 11. Plateau duration when the optical depth at the IB $\tau_{\text{IB}} = 10$, divided by plateau duration for the same explosion with no ^{56}Ni , as compared to the analytic scaling Equation (10) (red dashed line) with C_f determined from our fits. Color corresponds to M_{Ni} in units of solar masses. Deviations of each of the models from this relationship are shown in the bottom panel.

all of those models where the light curve has a clear end of plateau and nickel tail, we found that our fitting formula recovers a plateau that is 7%–20% shorter when using the values for M_{Ni} , M_{ej} , and E_{exp} reported in Dessart et al. (2013). This amounts to a difference of 8–27 days, with the worst agreement in the case of the low-metallicity (1/10 solar) model m15z2m3 and the best agreement in the case of their “new”

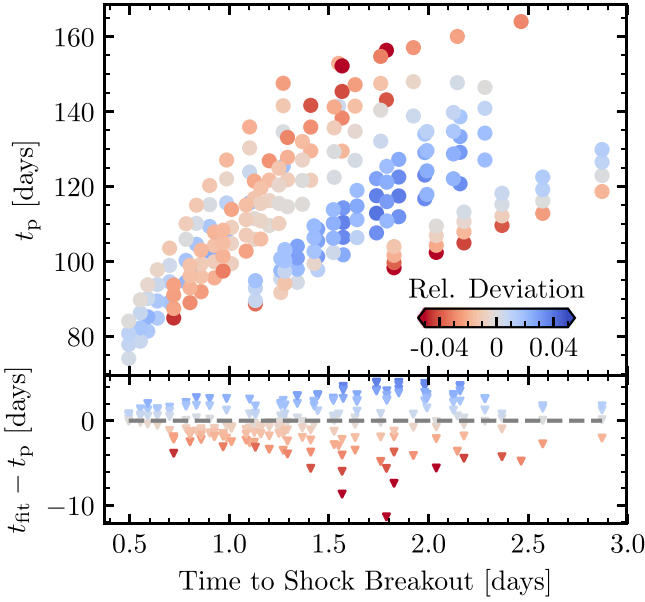


Figure 12. Plateau durations for our 218 SN light curves with $M_{\text{Ni}} \gtrsim 0.03 M_{\odot}$ (top panel) and the difference in plateau duration between the model t_p and the plateau duration t_{fit} extracted by applying Equation (12) to the M_{ej} , E_{exp} , and M_{Ni} of each model (bottom panel), colored by $(t_{\text{fit}} - t_p)/t_p$, the fractional deviation between t_p from the models and t_{fit} . The x -axis is the time the model takes to reach shock breakout.

s15N model. The rms difference in $|t_p - t_{\text{fit}}|$ is 18 days, about 14% relative to the average plateau in their models.

5.3. Constraining Explosion Parameters with ET

Following the work of Shussman et al. (2016a), Nakar et al. (2016), Kozyreva et al. (2018), and others, we can also express the impact of ^{56}Ni on t_p in terms of the ratio of the time-weighted energy contribution of the ^{56}Ni decay chain to the observable quantity ET. This ratio is defined in Nakar et al. (2016) as

$$\eta_{\text{Ni}} = \frac{\int_0^{t_p} t Q_{\text{Ni}}(t) dt}{\text{ET}}, \quad (13)$$

where

$$\text{ET} = \int_0^{\infty} t (L_{\text{bol}}(t) - Q_{\text{Ni}}(t)) dt \quad (14)$$

is the time-weighted energy radiated away that was generated by the initial shock and not by ^{56}Ni decay, and

$$Q_{\text{Ni}} = \frac{M_{\text{Ni}}}{M_{\odot}} (6.45 e^{-t/8.8 \text{ days}} + 1.45 e^{-t/113 \text{ days}}) \times 10^{43} \text{ erg s}^{-1} \quad (15)$$

is the instantaneous heating rate of the ejecta due to the decay chain of radioactive ^{56}Ni assuming complete trapping given in Nadyozhin (1994), and t is the time in days since the explosion. It is generally assumed that $L_{\text{bol}}(t) = Q_{\text{Ni}}(t)$ after the photospheric phase, on the nickel tail, and so the integral for ET is often expressed to be bounded at $t_{\text{Ni}} \approx t_p$. We find this to be valid; see the bottom panel of Figure 13.

Figure 13 shows the impact of ^{56}Ni on light curves and the integrated ET for the M16.3_R608 model exploded with $E_{\text{exp}} = 10^{51}$ erg at different M_{Ni} . The bottom panel gives the

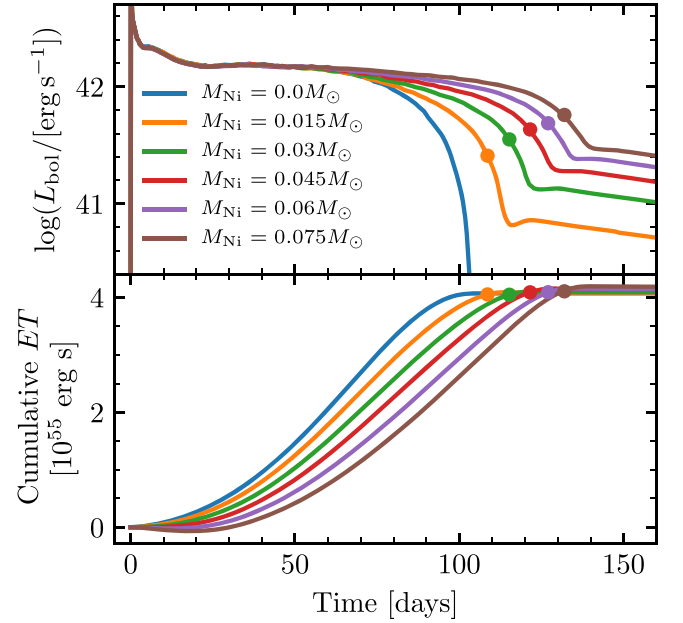


Figure 13. Impact of ^{56}Ni on L_{bol} (top panel) and cumulative ET integrated from shock breakout to the time on the x -axis (bottom panel) for the M16.3_R608 model exploded with $E_{\text{exp}} = 10^{51}$ erg and $M_{\text{Ni}}/M_{\odot} = 0.0, 0.015, 0.03, 0.045, 0.06, \text{ and } 0.075$. Circles indicate t_p for the events where $M_{\text{Ni}} > 0.0 M_{\odot}$.

cumulative ET, integrated from shock breakout to the time on the x -axis. Most of the contribution to ET comes from luminosity on the plateau, with little contribution at early times ($t < 20$ days) and no contribution from the nickel tail. In the very ^{56}Ni -rich case, the cumulative integral may dip slightly negative around day 20, as radiative cooling is briefly less efficient than heating from the ^{56}Ni decay chain ($L_{\text{bol}} < Q_{\text{Ni}}$ in this region). This is more pronounced in models exploded at lower energies. As expected, although heating from the radioactive decay chain of ^{56}Ni extends the plateau and elevates the nickel tail, it has very little impact on the final integrated value of ET calculated from our model light curves. Indeed, the variations of ET for the same explosion but different ^{56}Ni are at a few percent level.

Dimensionally, using the Popov scalings for L_{50} and plateau duration with no ^{56}Ni (t_0), ET is expected to scale as

$$\text{ET} \propto L_{50} t_0^2 \propto M_{\text{ej}}^{1/2} E_{\text{exp}}^{1/2} R, \quad (16)$$

and thus η_{Ni} should scale as M_{Ni}/ET . A more detailed derivation of this same scaling is given in Shussman et al. (2016a). This recovers the extension to the plateau duration given by Equation (10), recast as

$$t_{\tau=10}/t_0 = (1 + a \eta_{\text{Ni}})^{1/6}, \quad (17)$$

where the scaling factor a can be fit from models and encodes information about the internal structure of the ejecta, and in particular the concentration of ^{56}Ni . Kozyreva et al. (2018) find that for typical models $a \approx 4$ (their Figure 5). Figure 14 shows the extension of the plateau as a function of η_{Ni} in our models. We find slightly higher values for a , with more models falling along $a \approx 5.5$, indicating a larger impact of ^{56}Ni on the plateau duration, in part because η_{Ni} encodes information about ^{56}Ni mixing, and our models make use of the Duffell RTI

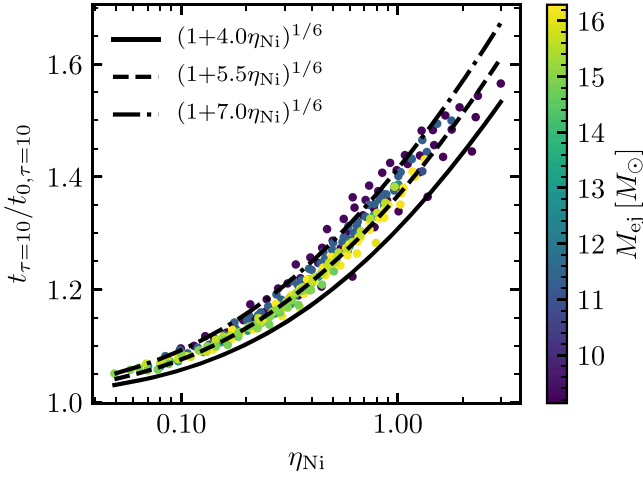


Figure 14. Plateau duration for models with ^{56}Ni relative to the same explosion with no ^{56}Ni , vs. the parameter η_{Ni} . Color corresponds to ejecta mass and can be used to distinguish between the individual progenitor models. Black lines correspond to the plateau extension factor $(1 + a\eta_{\text{Ni}})^{1/6}$ for different values of a .

prescription, whereas mixing is parameterized in Kozyreva et al. (2018). We show good agreement with the functional form in Equation (17).

For SNe with a reasonably well-sampled bolometric light curve where M_{Ni} is measured from the nickel tail, ET can be calculated and used to constrain M_{ej} , E_{exp} , and progenitor R for a given explosion. In addition, ET can provide a critical constraint for explosions with lower M_{Ni} , where the ^{56}Ni decay chain does not dominate the internal energy of ejecta and thus the simple power law of Equation (12) should not apply. Although observationally M_{Ni} must be extracted from the nickel tail in order to calculate ET, ET does not follow any scaling with M_{Ni} , as it subtracts the contribution of ^{56}Ni heating in the light-curve evolution.

To determine how ET scales with M_{ej} , E_{exp} , and R in our models, we use the same 218 model light curves as with t_p in Equation (12), to recover

$$\log(\text{ET}/\text{erg s}) = 55.460 + 0.299 \log(M_{10}) + 0.435 \log(E_{51}) + 0.911 \log(R_{500}) \quad (18)$$

for our suite of models, which does not include interactions CSM. This scaling has a slightly shallower dependence on M_{ej} , E_{exp} , and progenitor R than Equation (16). The agreement between our models and Equation (18) is shown in Figure 15. The rms deviations between our models are 5.0%, with a maximum deviation of 12.4%. Although the fit was performed on models with $M_{\text{Ni}} \gtrsim 0.03M_{\odot}$ to be consistent with our set of models for t_p , the recovered scaling applies similarly well for our models with $M_{\text{Ni}} < 0.03M_{\odot}$, with rms deviations of 5.3% and all deviations under 20%. The overlapping black rings in Figure 15 show the typical scatter in values of ET for the same explosion when varying M_{Ni} . Each set of overlapping rings corresponds to ET for a single progenitor model exploded with a single E_{exp} , but with different values of M_{Ni} . This scatter in ET when only varying M_{Ni} is well within the scatter between the models and the fitted Equation (18).

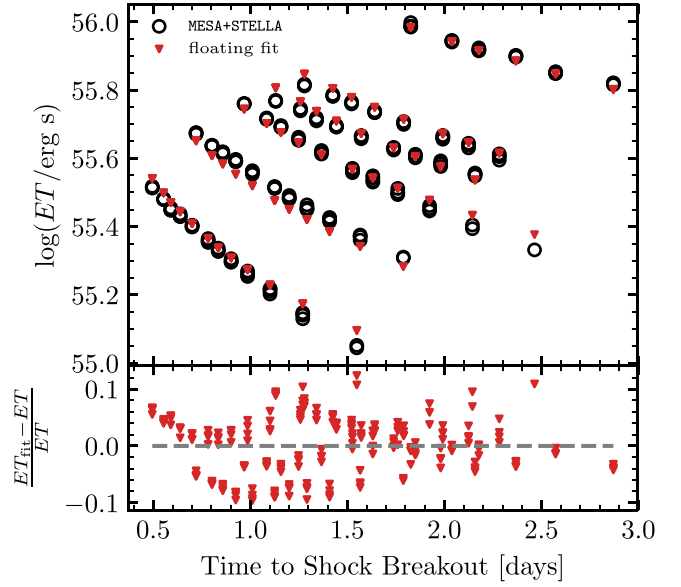


Figure 15. Calculated values of ET for 218 SN light curves and the values recovered with the fitted Equation (18) (top panel), and fractional deviations between ET in the models and recovered using Equation (18) (bottom panel).

6. Observed Velocity Evolution

We now discuss the diagnostic value of the material velocity inferred from the absorption minimum of the Fe II $\lambda 5169$ line, often measured and reported at day 50, $v_{\text{Fe},50}$. Ideally, the measured Fe line velocities would provide an additional quantitative measurement that would allow for estimation of progenitor and explosion properties (Pejcha & Prieto 2015a; Müller et al. 2017). However, as we show here, these measurements are highly correlated with bolometric luminosity measurements at a fixed time on the plateau and are largely redundant at day 50. If there is no substantial CSM around the star, then earlier time ($\lesssim 20$ days) measurements may prove more useful (see Section 7.2).

The Fe II $\lambda 5169$ velocity is typically used to approximate the velocity at the photosphere (v_{ph}), although there is substantial evidence that measured line velocities are typically higher than that predicted for the model photosphere ($\tau = 2/3$; e.g., Utrobin et al. 2017; MESA IV). In a homologously expanding medium, the strength of a given line is quantified using the Sobolev optical depth (Sobolev 1960; Castor 1970; Mihalas 1978; Kasen et al. 2006), which accounts for the shift in the line profile due to the steep velocity gradient in the ejecta. This is captured in MESA+STELLA following MESA IV, where the $\tau_{\text{Sob}} = 1$ condition is used to measure iron line velocities (v_{Fe}). Although in the following we discuss both this velocity and the velocity at the model photosphere, we recommend using v_{Fe} defined when $\tau_{\text{Sob}} = 1$ when comparing to observations.

6.1. Velocities in Explosion Models

When the velocity profile of the ejecta becomes fixed in time, this material is said to be in homologous expansion. Analytically, homology is often approximated as $r = vt$ for a fluid element at radial coordinate r with velocity v at time t . While not quite true for material in the center of the ejecta, which is expanding more slowly and therefore the initial radial coordinate is still relevant, this approximation generally holds for faster-moving material that has experienced more significant expansion at a given time, as

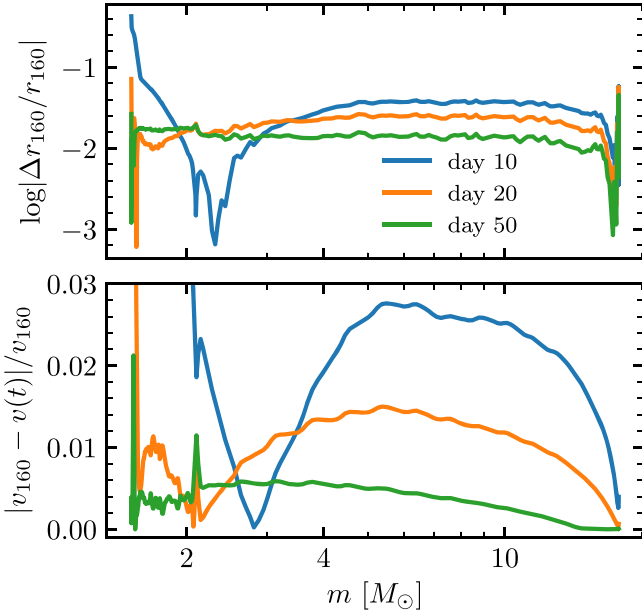


Figure 16. Agreement between hydrodynamical models and homologous expansion. The top panel shows the relative error in predicting the radial profile at day 160 by assuming homology starting at days 10, 20, and 50, compared to the true radial coordinate at day 160 in STELLA. The bottom panel shows the absolute relative deviation between the velocity profiles at days 10, 20, and 50 and the profile at day 160.

well as for the slower-moving material at late times when it is becoming visible. This is reflected in Figure 32 of MESA IV.

Many software instruments devoted to modeling radiative transfer, such as Sedona, assume homologous expansion in the true sense of a fixed velocity profile. Figure 16 shows the extent to which this is satisfied in our M16.3_R608 model exploded with 10^{51} erg. The top panel shows the relative error in predicting the radial coordinate of a fluid element at day 160 by assuming $r_h(\text{day}160) = r(t_0) + v(t_0)(160 \text{ days} - t_0)$ for homology starting at $t_0 = \text{days } 10, 20, \text{ and } 50$. We define $\Delta r_{160} = r_{160} - r_h(\text{day}160)$, where r_{160} is the true radius of that fluid element at day 160 in STELLA. The bottom panel shows the deviation between the velocity profiles at days 10, 20, and 50 and that at day 160. Before homology, the innermost material is moving slightly faster than its day 160 value, and the outer material is moving slightly slower. Even in the envelope, there is deviation between the day 10 velocity profile and day 160 at the level of a few percent. By day 20 this falls below 2%, and by day 50 typical deviations of the velocity profile in the bulk of the ejecta from the velocity profile at day 160 are at the level of 0.5%. Generally, by day 20, the difference in predicted radial coordinate of the half-mass fluid element at day 160 is below 3% of its true value in the hydrodynamical simulation. At this time the radial coordinate predicted for day 50 is also within 2% of its true value at day 50.

Figure 17 shows approximately homologous velocity profiles (taken here at day 50) scaled by the square root of E_{exp} for all six progenitor models at all energies that cause sufficiently little fallback. Each family of colored lines reflects explosions of an individual model, and each of the six families of lines contains the profiles for multiple explosion energies for that model. When looking at any fixed mass coordinate within a single progenitor model, the fluid velocity divided by $\sqrt{E_{\text{exp}}}$

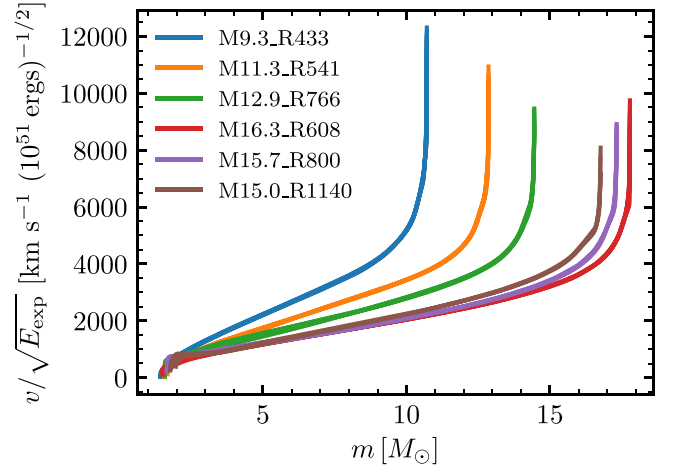


Figure 17. Day 50 velocity profiles in STELLA, divided by the square root of E_{exp} , vs. mass coordinate for six unique progenitor models with a variety of explosion energies. Each colored line represents a different model and lies on top of a collection of 6–12 nearly identical lines that correspond to different explosion energies for the same progenitor model.

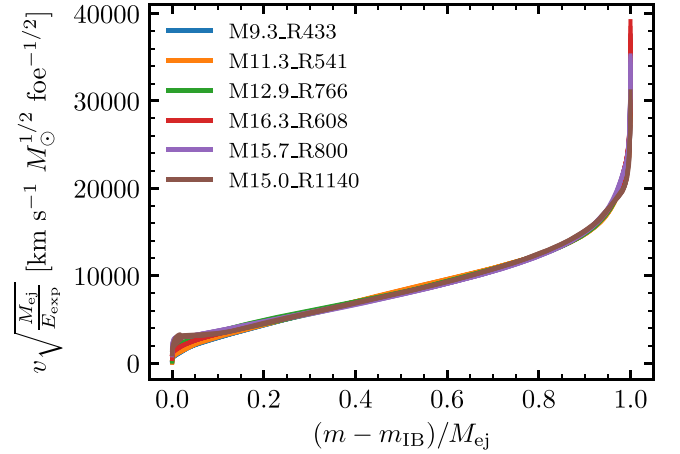


Figure 18. Day 50 velocity profiles in STELLA, multiplied by $\sqrt{M_{\text{ej}}/E_{\text{exp}}}$, vs. dimensionless ejecta mass coordinate for all 57 explosions with energies sufficient to yield little fallback. For a fixed fractional position within the ejecta, velocities obey the scaling in Equation (19).

is constant. Moreover, as shown in Figure 18, looking at the same dimensionless mass coordinate inside the ejecta and scaling also by the square root of M_{ej} , this relationship holds for any dimensionless ejecta mass coordinate throughout the entire velocity profile, with small variations only near the IB, where the reverse shock becomes relevant and where fallback has a greater effect.

Popov (1993), Pejcha & Prieto (2015a), and others have often assumed that

$$E_{\text{exp}} \approx \frac{1}{2} M_{\text{ej}} v_{\text{Ph},50}^2, \quad (19)$$

where $v_{\text{Ph},50}$ is the photospheric velocity at day 50, in order to close the system of equations for L_{50} and t_p as a function of M_{ej} , E_{exp} , and progenitor radius R . While the scaling law suggested in Equation (19) holds for the fluid velocity at a fixed dimensionless ejecta mass coordinate, as shown in Figure 18, as the photosphere moves deeper into the ejecta, it does not probe velocities at the same mass coordinate at a given time

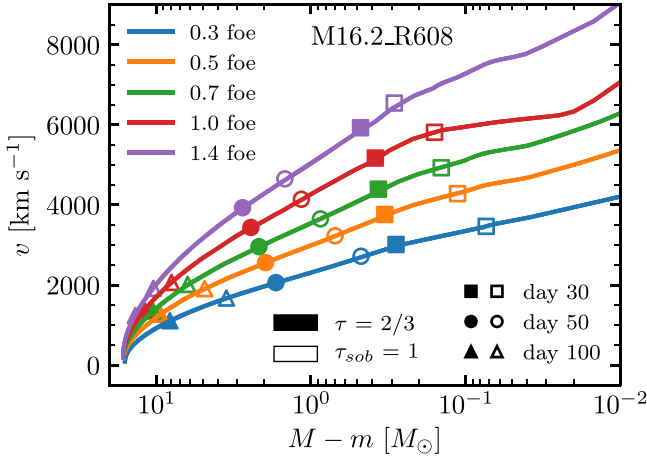


Figure 19. Day 50 velocity profiles vs. overhead mass coordinate in STELLA for our M16.3_R608 model at five different explosion energies. We have included photospheric (filled markers) and Fe II $\lambda 5169$ line velocities (open markers) for days 30, 50, and 100 as denoted by the shape of the marker.

after shock breakout. Rather, at a fixed time in the evolution, faster-expanding ejecta in higher-energy explosions allow the observer to see deeper mass coordinates, compared to a lower-energy explosion of the same star. This is evident in Figure 19, which shows velocity profiles for the M16.3_R608 model at five different explosion energies, marking the location of the photosphere and Fe II $\lambda 5169$ line at fixed times. As a result of the expanding ejecta, we expect a shallower scaling for velocity as a function of energy at fixed mass than the naive $v_{\text{Ph},50} \propto E_{\text{exp}}^{1/2}$. Indeed, a linear fit for a single model with fixed ejecta mass and radius finds shallower scalings: $v_{\text{Ph},50} \propto E_{\text{exp}}^{0.36}$, and $v_{\text{Fe},50} \propto E_{\text{exp}}^{0.30}$. These scalings approximately hold for the other individual models.

Additionally, a simple velocity scaling with M_{ej} and E_{exp} becomes murkier when comparing across models of different masses at fixed explosion energy, since there is no reason for the same explosion energy to yield the “same” mass coordinate at the same time in two different progenitors. In fact, as seen in Figure 20, v_{Fe} and v_{Ph} at day 50 are not even monotonic in M_{ej} for different stars at fixed E_{exp} . Thus, we cannot derive any power law for $v_{\text{Ph},50}$ or $v_{\text{Fe},50}$ solely as a function of M_{ej} and E_{exp} . As we show in the following section, additional dependences are relevant (Equation (20)).

6.2. L_{50} – $v_{\text{Ph},50}$ Relation

This result highlights a true degeneracy, discovered observationally by Hamuy (2003) and explained by Kasen & Woosley (2009). We start with the Stefan-Boltzmann formula for luminosity, $L = 4\pi R_{\text{phot}}^2 \sigma T_{\text{eff}}^4$, where R_{phot} is the photospheric radius, and note that T_{eff} is roughly constant at the photosphere and set by H recombination to $T_{\text{eff}} \approx 6000$ K. At fixed time on the plateau, (e.g., day 50), while the ejecta is expanding homologously with radial position $r \approx vt$ for any given mass coordinate, for the photosphere at day 50 $L_{50} \propto v_{\text{Ph},50}^2$ and so $v_{\text{Ph},50} \propto \sqrt{L_{50}}$. In this way, the luminosity, together with homologous expansion, sets the location of the photosphere within the expanding ejecta, which in turn sets the velocity measured at or near the photosphere.

Figure 21 shows $v_{\text{Ph},50}$ and $v_{\text{Fe},50}$ versus L_{50} for all 57 explosions that experience sufficiently little fallback (six

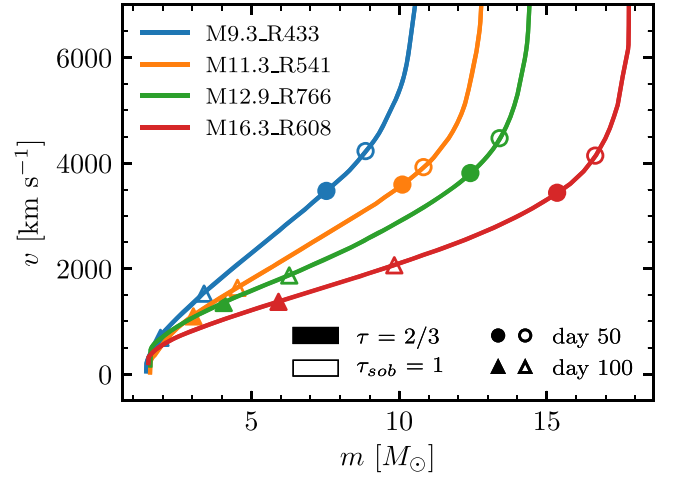


Figure 20. Day 50 velocity profiles for four different models all exploded with an energy of 1.0×10^{51} erg. Filled markers indicate the location of the photosphere, and open markers indicate where the Fe II $\lambda 5169$ line is formed. Velocities at days 50 and 100 are denoted by the shape of the marker.

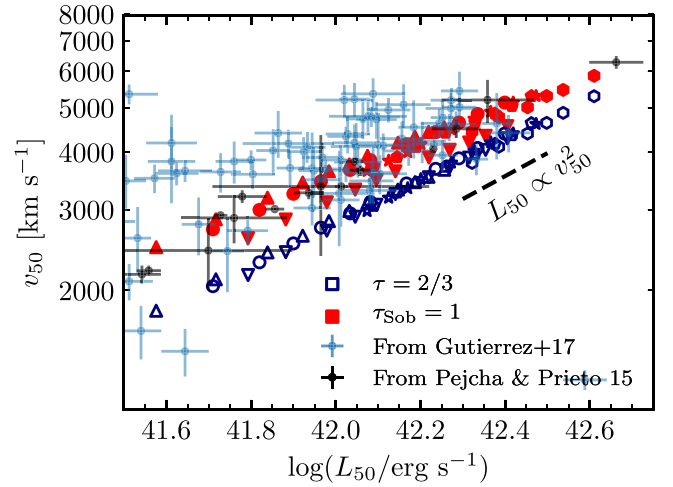


Figure 21. Velocity vs. luminosity at day 50 for a variety of progenitor models and explosion energies. Open navy blue markers denote photospheric velocities ($\tau = 2/3$), and closed red markers denote Fe II $\lambda 5169$ velocities ($\tau_{\text{sob}} = 1$). Points with error bars are data from two samples: Gutiérrez et al. (2017) (blue) and Pejcha & Prieto (2015a) (black).

models with 6–12 explosion energies each). Also plotted are data from Pejcha & Prieto (2015a) and Gutiérrez et al. (2017).⁶ In both observational data sets, velocities are inferred from the Fe II $\lambda 5169$ line, suggesting that Fe II $\lambda 5169$ line velocities are better captured in our models at $\tau_{\text{sob}} \approx 1$, rather than assuming that the line is formed at the photosphere ($\tau = 2/3$). We also see good agreement between our models and the scaling $v_{\text{Ph},50} \propto \sqrt{L_{50}}$.

It is therefore unsurprising that the Fe velocities during the plateau phase match the data for a model with a luminosity match at day 50. This was seen in Section 6 of MESA IV,

⁶ Luminosities from Pejcha & Prieto (2015a) are bolometric luminosities provided by O. Pejcha (2017, private communication). Luminosities from Gutiérrez et al. (2017) were estimated from M_V measurements at day 50 provided by C. Gutiérrez (2018, private communication), assuming negligible bolometric correction $BC \approx 0$ for M_V following the correction for SN 1999em on the plateau, shown in Bersten & Hamuy (2009). Typical V-band bolometric corrections on the plateau of SNe IIP are $BC \approx -0.15$ to 0.1, and the variation in $\log L_{50}$ from assuming a BC of 0 versus other values within that range is smaller than the error bars on the data.

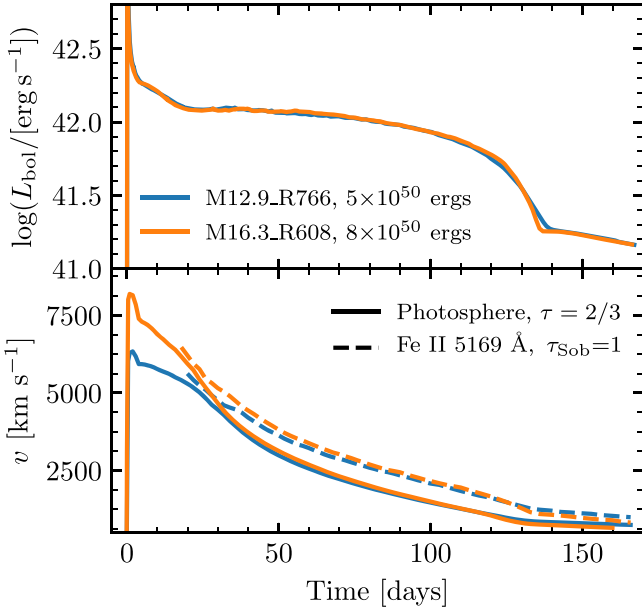


Figure 22. Luminosity and velocity for the 99em_16 (renamed M12.9_R766) and 99em_19 (renamed M16.3_R608) models from Paxton et al. (2018) with different explosion energies in order to attain light-curve agreement.

Figure 42, where two models with light-curve agreement with SN 199em show identical velocity evolution. Figure 22 shows the luminosity and velocity of those two progenitor models, renamed M12.9_R766 and M16.3_R608 in our suite, blown up with slightly adjusted explosion energies to produce even better light-curve agreement. In the case where models match closely in both L and t_p , the agreement in velocity is excellent throughout the evolution of the SN.

As with L_{50} in Section 4, we fit a power law for v_{50} as a function of M_{ej} , E_{exp} , and R to our models with constant nickel mass $M_{\text{Ni}} = 0.03M_{\odot}$. We do this with both $v_{\text{Fe},50}$ and $v_{\text{ph},50}$ at day 50, noting that observationally $v_{\text{Fe},50}$ is the relevant scaling. For the photospheric velocity at day 50, we found power laws that are very similar to the scaling found if $v_{\text{ph},50} \propto L_{50}^{1/2}$:

$$\begin{aligned} \log(v_{\text{ph}}/\text{km s}^{-1}) &= 3.54 - 0.19 \log M_{10} + 0.36 \log E_{51} + 0.32 \log R_{500}, \end{aligned} \quad (20)$$

where the prefactor and power-law coefficients are all fit from our models.

This is valuable insofar as it reinforces the degeneracy highlighted in Figures 21 and 22, but, as discussed, this velocity is unmeasurable, and observed Fe II $\lambda 5169$ line velocities are better estimated by ($\tau_{\text{Sob}} = 1$). A similar fit to v_{Fe} at day 50,

$$\begin{aligned} \log(v_{\text{Fe},50}/\text{km s}^{-1}) &= 3.61 - 0.12 \log M_{10} + 0.30 \log E_{51} + 0.25 \log R_{500}, \end{aligned} \quad (21)$$

yields higher predicted velocities everywhere and shows somewhat shallower dependence on each of the explosion properties. The model Fe line velocities and their residuals as compared with Equation (21) are shown in Figure 23.

Although the degeneracy is less pronounced for $\tau_{\text{Sob}} = 1$ than for the photosphere, with some scatter in Figure 21 and differences in the recovered power laws, this scatter is small

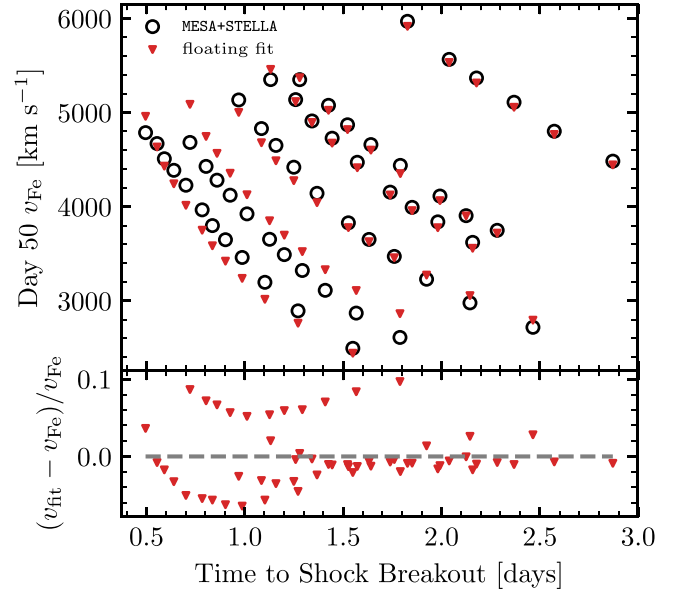


Figure 23. Model v_{Fe} ($\tau_{\text{Sob}} = 1$) at day 50, and velocities recovered with the fitting formulae (top panel) and their residuals (bottom panel) for our suite of 57 explosions with $M_{\text{Ni}} = 0.03M_{\odot}$. So as to clarify the model space, we use time to shock breakout as the x -axis.

compared to intrinsic variations in luminosity and plateau duration and is therefore insufficient to break the degeneracy between v and L in order to provide accurate estimates for M_{ej} , E_{exp} , and R . It is for this reason that we do not advocate using measured velocities at day 50 to infer explosion properties.

7. Families of Explosions

7.1. Inverting Our Scalings

Due to the degeneracies highlighted in Section 6, we cannot simply extract M_{ej} , E_{exp} , and R from light-curve measurements and $v_{\text{Fe},50}$. Attempting to invert all three scalings (Equations (8), (12), and (18)) is ill-conditioned and within the scatter within our models. However, we can use the scalings to solve for two of the three relevant explosion properties as a function of the third, revealing a family of possible explosions that yield nearly identical bolometric light curves.

SNe with direct progenitor observations are improving with time, so we solve Equations (8) and (12) for M_{ej} and E_{exp} as a function of M_{Ni} , L_{50} , t_p , and R , to find

$$\begin{aligned} \log(E_{51}) &= -0.728 + 2.148 \log(L_{42}) - 0.280 \log(M_{\text{Ni}}) \\ &\quad + 2.091 \log(t_{p,2}) - 1.632 \log(R_{500}), \\ \log(M_{10}) &= -0.947 + 1.474 \log(L_{42}) - 0.518 \log(M_{\text{Ni}}) \\ &\quad + 3.867 \log(t_{p,2}) - 1.120 \log(R_{500}), \end{aligned} \quad (22)$$

where M_{Ni} is in units of M_{\odot} , $L_{42} = L_{50}/10^{42} \text{ erg s}^{-1}$, and $t_{p,2} = t_p/100$ days. Alternatively, we can use a measured ET rather than t_p to find

$$\begin{aligned} \log(E_{51}) &= -0.587 - 1.497 \log(R_{500}) \\ &\quad + 1.012 \log(\text{ET}_{55}) + 0.756 \log(L_{42}), \\ \log(M_{10}) &= -0.685 - 0.869 \log(R_{500}) \\ &\quad + 1.872 \log(\text{ET}_{55}) - 1.101 \log(L_{42}), \end{aligned} \quad (23)$$

where $\text{ET}_{55} = \text{ET}/10^{55} \text{ erg s}$.

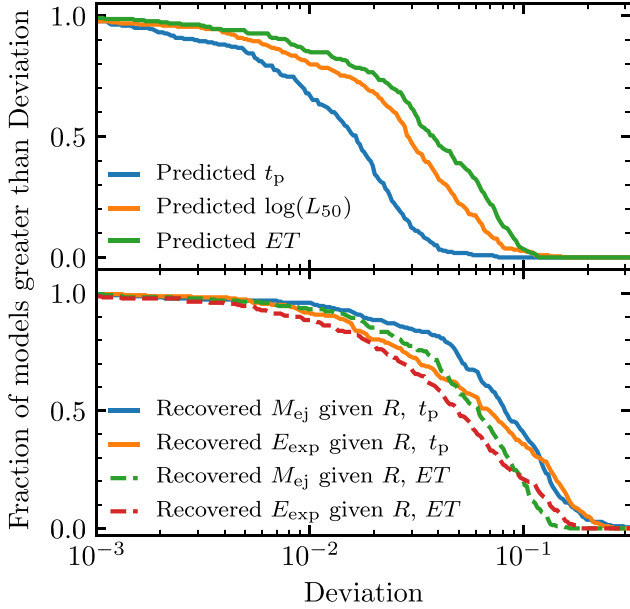


Figure 24. Distribution of deviations between our models and Equations (8) and (12) (top panel), and the distribution of deviations between recovered values of M_{ej} and E_{exp} by applying the inverted scalings (Equation (22)) to the model light-curve properties and radii, and the models themselves (bottom panel). This gives a heuristic for the agreement between the fitted formulae and our suite of models.

Before demonstrating how to apply these fitting formula to observed SNe, we show how well modeled events can be matched. The top panel of Figure 24 shows the fraction of models with light-curve properties matching their fitted values (applying Equations (8), (12), and (18)) within a given deviation tolerance shown on the x -axis. The bottom panel shows the fraction of models in which we can recover the values of M_{ej} and E_{exp} within a given deviation tolerance by applying Equation (22) (solid lines) or Equation (23) (dashed lines) to the model light-curve observables and R . Given that there is no statistical meaning to the sample of models beyond probing different regions of parameter space, this merely provides a heuristic guide to how well our sample of models matches with the fitted formulae. Applying Equation (22) using t_p to our suite of nickel-rich SNe, we recover M_{ej} and E_{exp} with rms deviations between the models and the fits of 10.7% and 10.4%, respectively, with maximum deviations of 35% and 27%. Using ET and Equation (23), we recover M_{ej} and E_{exp} with rms deviations between the models and the fits of 7.3% and 7.6%, respectively, with maximum deviations of 16% and 18%. Although the modeling uncertainties for the inverted ET scalings are smaller than those that use t_p , the observable uncertainty is greater and may be accompanied by an offset, as excess emission within the first 10–40 days due to interaction with CSM may cause an excess in ET as compared to our models.

Using these relations, we now show how very comparable light curves (and thus comparable Fe II $\lambda 5169$ line velocities on the plateau) can be produced with different progenitors exploded at different energies. Figure 25 shows an example of the family of models in $M_{\text{ej}}-E_{\text{exp}}$ parameter space as a function of R that could produce an “observed” SN light curve with $\log(L_{50}/\text{erg s}^{-1}) = 42.13$, $\log(\text{ET}/\text{erg s}) = 55.58$, $t_p = 123$, and $M_{\text{Ni}} = 0.045M_{\odot}$, which are the values matching a randomly

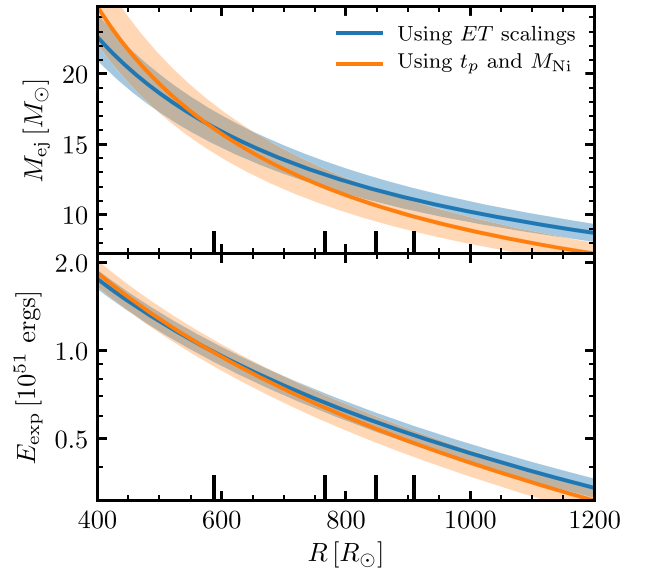


Figure 25. Degeneracy curves applying Equation (22) (orange) and Equation (23) (blue) as a function of progenitor radius R for an “observed” SN with $\log(L_{50}/\text{erg s}^{-1}) = 42.13$, $\log(\text{ET}/\text{erg s}) = 55.58$, $t_p = 123$, and $M_{\text{Ni}} = 0.045M_{\odot}$. The shaded region corresponds to the rms deviations between our models and the values recovered by applying Equations (22) and (23). Short black lines correspond to the radii of the M17.8_R587, M12.9_R766, M10.2_R848, and M9.8_R909 models, which produce the light curves, velocities, and ET evolution shown in Figure 26.

selected model out of our suite: the M12.9_R766 model exploded with $E_{\text{exp}} = 6 \times 10^{50}$ erg and that M_{Ni} .

To exhibit how this exercise would proceed, we constructed three additional models consistent with the bands in Figure 25, based on Equation (22) using t_p . We then explode these progenitor models with E_{exp} as dictated by the degeneracy curve. We created multiple such models: one with $M_{\text{ej}} = 17.8M_{\odot}$ and $R = 587R_{\odot}$, which we explode with 1×10^{51} erg, one with $M_{\text{ej}} = 10.2M_{\odot}$ and $R = 848R_{\odot}$, which we explode with 5×10^{50} erg, and one with $M_{\text{ej}} = 9.8M_{\odot}$ and $R = 909R_{\odot}$, which we explode with 4.5×10^{50} erg. The values of R for these three models, and for M12.9_R766 exploded with 6×10^{50} erg, are shown as black tick marks in Figure 25. Figure 26 shows the resulting light curves, velocities, and accumulated ETs. We see very good agreement in L_{50} and along the plateau and recover t_p values from 120 to 125 days for all four light curves.

The values of ET for three of the four light curves agree within $\approx 2\%$, ranging from 3.75 to 3.84×10^{55} erg s; however, the 5×10^{50} erg explosion of the M10.2_R848 model has a value of ET that is noticeably higher, at 4.26×10^{55} erg s. Additionally, velocities agree on the plateau and thus cannot be used to break the light-curve degeneracy, which at least spans a factor of 2 in explosion energy, nearly a factor of 2 in M_{ej} , and a factor of 1.5 in progenitor R . This captures much of the parameter space in which SNe IIP from RSG progenitors could be produced to begin with!

7.2. The Importance of Velocities at Early Times

Although velocity measurements at day 50 are largely degenerate with measurements of L_{50} , as discussed in detail in Section 6, early-time velocities up to day ≈ 20 could be used to distinguish between low-energy explosions of large-radius, lower-mass RSGs

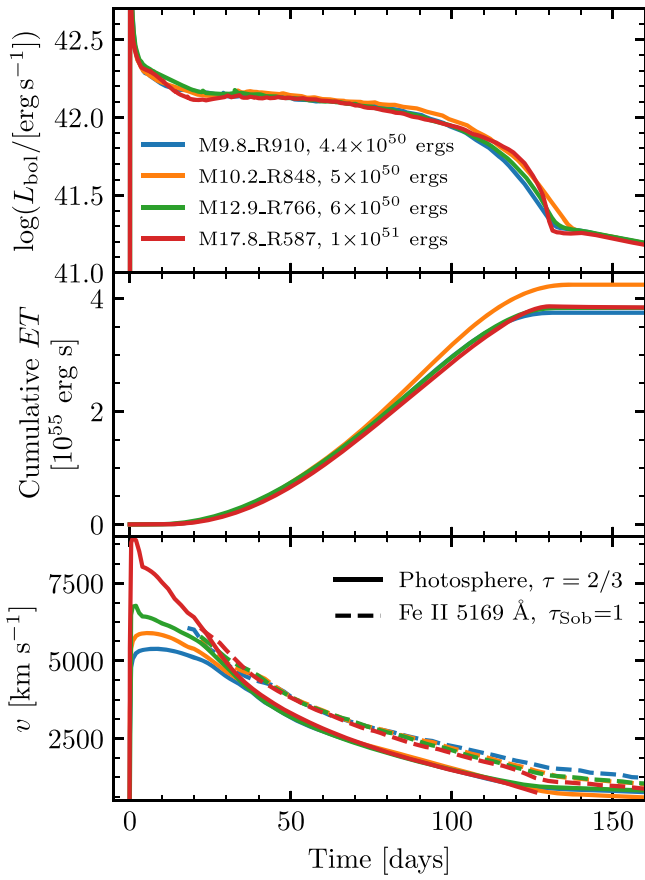


Figure 26. Light curves, cumulative ET, and velocities for four different explosions that yield nearly the same L_{50} , t_p , and velocities at day 50.

and high-energy explosions of compact-radius, high-mass RSGs in cases where there is minimal CSM present. As seen in the bottom panel of Figure 26, higher-energy explosions of compact stars yield faster velocities at early times. Before around day 20, the radial coordinate of the photosphere is moving outward, and the declining photospheric temperature is set by shock cooling rather than by recombination. Thus, in this phase the velocity measured near the photosphere is not dictated by the plateau luminosity as it is at day 50. Early light curves and photospheric velocities are discussed in detail by Morozova et al. (2016) and Shussman et al. (2016b). Shussman et al. (2016b) find an expression for the photospheric velocity at early times as a function of M_{ej} , E_{exp} , and R (their Equation (48)), assuming that the density profile of the progenitor model behaves like a power law in radial coordinates. After the photosphere leaves the so-called breakout shell (5 days $\lesssim t \lesssim 20$ days), Shussman et al. (2016b) find that $v_{ph}(t)/\text{km s}^{-1} \approx 1.2 \times 10^4 M_{15}^{-0.3} E_{51}^{0.38} R_{500}^{-0.14} t_d^{-0.2}$, where $M_{15} = M_{ej}/15M_{\odot}$ and $t_d = t/\text{days}$. At day 15 this equation describes our full suite of models with rms deviations of 5.5% and with all deviations under 15%.

As is also seen in Figure 2 of Morozova et al. (2016), no single power law fully describes progenitor density profiles around the photospheric mass coordinate in our models for any fixed time in the light-curve evolution. Nonetheless, our entire suite of models, which does not include the presence of CSM,

can approximately be described by the fitted power law

$$\log(v_{\text{Ph},15}) = 3.90 - 0.22 \log(M_{10}) + 0.43 \log(E_{51}) - 0.13 \log(R_{500}), \quad (24)$$

where $v_{\text{Ph},15}$ is the photospheric velocity at day 15 in km s^{-1} , with rms deviations of 3.7% and a maximum deviation of 10% between the models and Equation (24). The dynamic range in $v_{\text{Ph},15}$ in our models is a factor of ≈ 3 , in the range of ≈ 4000 – $12,000 \text{ km s}^{-1}$.

Although Equation (24) and Shussman’s Equation (48) describe our models well, we warn the reader that velocities at this time are sensitive to the density structure of the outermost ejecta, including any asphericity, as well as any interactions with any CSM present. Thus, more work is needed in order to faithfully capture the early-time velocities and their dependence on the relevant properties of the explosion, especially in cases where CSM is present. Nonetheless, early-time velocity measurements could in principle provide a third constraint and break the light-curve degeneracies, thus allowing an inference of M_{ej} , progenitor R , and E_{exp} for a given observed SN IIP.

8. Concluding Remarks

We have shown the utility of using MESA+STELLA to model an ensemble of SN IIP progenitors, a capability introduced by Paxton et al. (2018). We introduced new best-fit scaling laws for the plateau luminosity at day 50, L_{50} (Equation (8)), and for the duration of the plateau t_p in the limit of nickel-rich ($M_{\text{Ni}} \geq 0.03M_{\odot}$) events (Equation (12)) as a function of ejecta mass, explosion energy, and progenitor radius. We also recovered a similar fit for the observable ET (Equation (18)). Velocity measurements on the plateau cannot be simply described by $v_{\text{Ph},50} \approx (2E_{exp}/M_{ej})^{1/2}$ assumed by Popov (1993) or the scaling given in Litvinova & Nadyozhin (1983), but rather scale with L_{50} as noted by Hamuy (2003), Kasen & Woosley (2009), and others, shown in our Figure 21. While early-time velocities observed during the photospheric phase (\approx day 15) could provide a promising third independent constraint on M_{ej} , E_{exp} , and R , these velocities can be affected by interaction with CSM, deviations from spherical symmetry, and the specifics of the density profile of the progenitor star. Thus, early velocities require more work in order to simply interpret in observed systems. Currently, given a bolometric light curve, one can at best recover a family of explosions that produce comparable light curves and thereby velocities on the plateau, as demonstrated in Figures 22 and 26. This can then be used to guide modeling efforts, especially when coupled with other constraints, such as a measurement of the core mass and thereby progenitor mass at the time of explosion (as in Jerkstrand et al. 2012). With a clear independent constraint on one explosion parameter, such as an observed progenitor radius, the other explosion properties can be simply recovered to around 15%.

We thank Josiah Schwab for guidance interpreting STELLA output and for formative conversations, Evan Bauer for discussions and comments on the original draft of the manuscript, and Dan Kasen for extremely helpful discussions. We also thank Claudia Gutierrez and Ondrej Pejcha for graciously providing data and Luc Dessart for providing models to compare to. This research benefited from interactions

with Maria Drout, Paul Duffell, Jim Fuller, Sterl Phinney, Eliot Quataert, and Todd Thompson that were funded by the Gordon and Betty Moore Foundation through grant GBMF5076. It is a pleasure also to thank Azalee Boestrom, Daichi Hiramatsu, Viktoriya Morozova, and Stefano Valenti for discussions and correspondences about observations. Lastly, we thank the anonymous referee for constructive comments that helped improve this manuscript.

J.A.G. is supported by the National Science Foundation Graduate Research Fellowship under grant No. 1650114. The MESA project is supported by the National Science Foundation (NSF) under the Software Infrastructure for Sustained Innovation program grant ACI-1663688. This research was supported in part by the Gordon and Betty Moore Foundation through Grant GBMF5076 and at the KITP by the NSF under grant PHY-1748958.

This research made extensive use of the SAO/NASA Astrophysics Data System (ADS).

Software: MesaScript (Wolf et al. 2017), Python from python.org, `py_mesa_reader` (Wolf & Schwab 2017), `ipython/jupyter` (Pérez & Granger 2007; Kluyver et al. 2016), `SciPy` (Jones et al. 2001), `NumPy` (van der Walt et al. 2011), and `matplotlib` (Hunter 2007).

Appendix A

Quantifying Fallback in Core-collapse Supernovae

Here we discuss modifications relative to MESA IV, of MESA modeling of the ejecta evolution after core collapse in massive stars (roughly $M > 8M_{\odot}$). These are focused on cases where the total final explosion energy is positive but insufficient to unbind the entirety of the material that does not initially collapse into the compact object. In these weak explosions, there is some amount of fallback material that does not become unbound. Our emphasis here is to quantify and remove fallback in model explosions of RSG progenitor stars. Although we describe models of SN IIP explosions, this scheme can be similarly applied to core-collapse events in massive stars that have lost the majority of their outer hydrogen envelope, which produce SNe Iib and Ib.

In MESA IV, three options existed to treat fallback:

1. Set the velocity of all inward-moving material with negative total energy to be zero, which creates a hydrostatic shell that can be excised from the ejecta before handing off to the radiation hydrodynamics code STELLA to calculate SN observables.
2. During the shock propagation phase, remove material at the IB if it has negative velocity (i.e., if it is infalling).
3. Remove material at the IB if it is moving with negative velocity and also has net negative energy (i.e., it is bound and infalling).

However, triggering fallback based only on conditions in the innermost zone can lead to problems. For example, in many models at lower explosion energies, while the innermost zone may have negative cell-centered velocity, it can be in thermal contact with neighboring zones. Therefore, to remove cells solely based on their having negative velocity creates a vacuum at the IB that can remove energy and mass that could otherwise remain in the ejecta. Moreover, energy deposited at the IB by any inward-propagating shock can cause the innermost zones to have positive total energy, while being surrounded by a larger amount of material with net negative energy. Because of

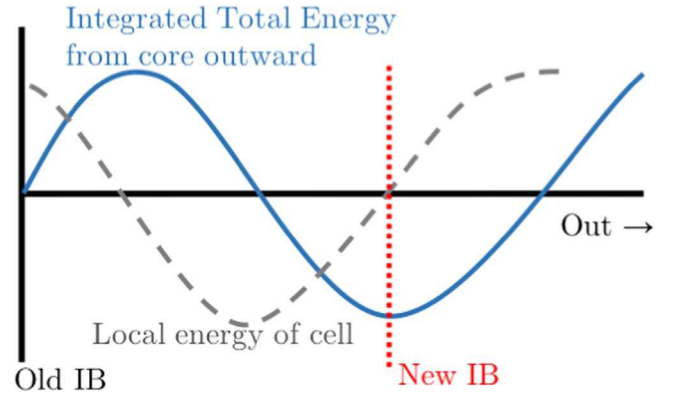


Figure 27. Diagram for new fallback criterion at a time step where there is net positive energy near the IB but a larger, gravitationally bound region above it that will eventually fall back.

this, in some models, checking only if the innermost zone is bound before triggering fallback can lead to bound material piling up on top of a small number of cells with positive total energy. If not removed, this can lead to a globally bound hydrostatic shell building up in the center, which might interact with the ejecta and affect concentrations of important species such as H and ^{56}Ni , thus affecting SN properties. Such a region can also lead to numerical problems if not properly excised before handing off to radiative transfer codes such as STELLA.

Paxton et al. (2019) (MESA 5) introduces two new user controls to better account for material that could fall onto the central object during the hydrodynamical evolution of low explosion energy core-collapse SNe. First, a new criterion is implemented to select which material is excised from the model.⁷ At each time step, MESA calculates the integrated total energy from the innermost cell to cell j above it:

$$E_j = \sum_{i=\text{inner}}^j \left[e_i - \frac{Gm_i}{r_i} + \frac{1}{2}u_i^2 \right] dm_i, \quad (25)$$

where for cell i at mass m_i and radius r_i , e_i is the internal energy in erg g^{-1} and u_i is the velocity in cm s^{-1} . If $E_j < 0$, then there is a bound inner region, and MESA continues this calculation outward until it reaches a cell k with local positive total energy ($e_k - Gm_k/r_k + u_k^2/2 > 0$), causing the integral to be at a local minimum. MESA deletes material inside this zone and moves the IB, fixing the inner radius of zone k to be the new radius of the IB `r_center`, and setting the velocity at the IB `v_center` = 0. A schematic diagram of this calculation, in a case where fallback is triggered but the innermost zones are unbound, is shown in Figure 27.

Figure 28 shows the evolution of the IB for explosions of varying total energy just after the explosion (E_{tot} , defined in Section 2), using the new fallback criterion for the M12.9_R766 progenitor model, which has a total energy of -4.4×10^{50} erg just before the explosion. Nearly all of the mass lost to fallback occurs while the forward-moving shock is in the helium layer, beginning around the time that the reverse shock generated at the interface between the CO/He layers reaches the IB. Because the new fallback prescription sets `v_center` = 0 and fixes `r_center` except in the case of fallback being triggered, all changes in the radius of the IB are

⁷ This criterion is triggered when `fallback_check_total_energy` is set to `.true.` in `star_job`.

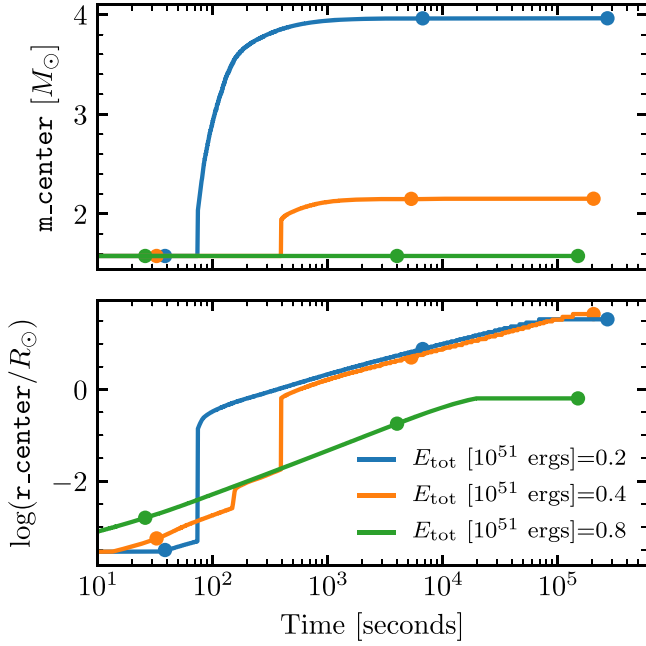


Figure 28. Evolution of the mass (top panel) and radial (bottom panel) coordinate of the IB for the new fallback prescription for the M12.9_R766 progenitor model from MESA IV for explosions of increasing energy. Colored circles correspond to times at which the forward shock crosses a sharp compositional gradient: entering the He layer, entering the H layer, and shock breakout. Because the fallback prescription holds r_{center} fixed and $v_{\text{center}} = 0$, all changes in r_{center} result from inner cells being removed from the model.

due to cells being removed from the IB. For sufficiently large explosion energies, little to no fallback is seen, although some cells of negligible mass are removed from the IB, causing the radius of the IB to move outward.

Second, in order to remove any slow-moving, nearly hydrostatic material left near the IB as a result of the fixed r_{center} , which may cause problems after handing off to radiation hydrodynamic codes (see Figure 30), MESA allows the user to specify a minimum innermost velocity for material that gets included in the final ejecta profile that is handed off to STELLA.⁸ MESA will then exclude all material beneath the innermost zone that has velocity greater than this velocity cut. This can lead to a small amount of additional mass that is excluded from the final ejecta profile at handoff.

The result of both modifications is shown in Figure 29, for three different models exploded at 12 different explosion energies. This can be loosely compared with Figure 6 of Perna et al. (2014). Included are the M12.9_R766 and M11.3_R541 models from our standard suite, as well as an additional model, named M20.8_R969, which has binding energy -8.4×10^{50} erg just before the explosion, included in order to demonstrate an explosion in a more massive star where there would be more fallback material due to more strongly bound core material. Generally, models with and without a velocity cut end with roughly the same amount of fallback. In cases where the explosion energy is just barely enough to unbind all of the mass, the velocity cut can remove a small additional amount of material. However, as seen in Figure 30, even in this case, a

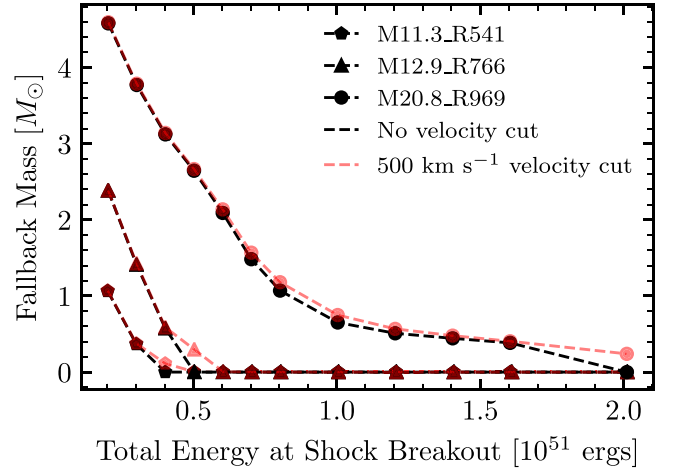


Figure 29. Mass of fallback material at shock breakout as a function of the total energy of the exploded model at the time of shock breakout for three different progenitor models exploded with 12 different explosion energies. Results are shown for the new integrated energy fallback criterion with no additional velocity cut (black points) and the same criterion with a 500 km s^{-1} velocity cut at shock breakout (red points).

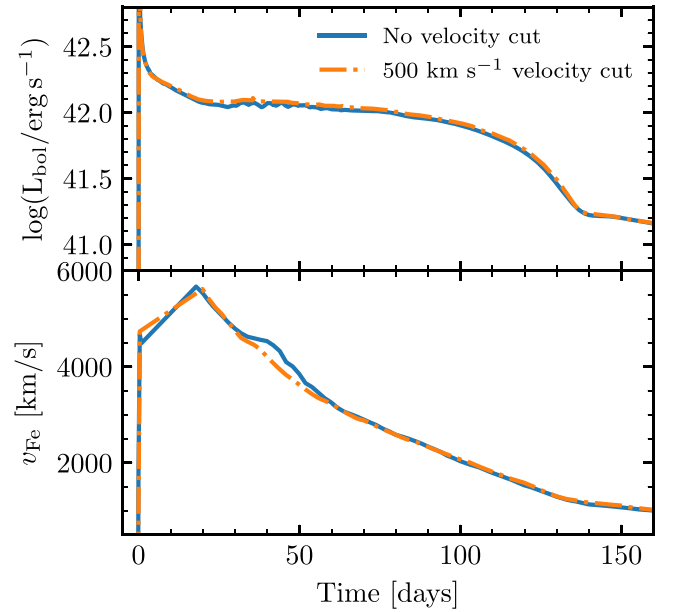


Figure 30. Effects of a velocity cut on STELLA light curves and Fe II $\lambda 5169$ line velocities for our M12.9_R766 progenitor model exploded with $E_{\text{tot}} = 5.0 \times 10^{51}$ erg and a nickel mass $M_{\text{Ni}} = 0.042 M_{\odot}$, where we see a noticeable difference between the mass of fallback material with and without a velocity cut ($\approx 0.3 M_{\odot}$).

suitable velocity cut between 100 and 500 km s^{-1} has very little effect on light-curve properties and the photospheric evolution of the SN and can greatly reduce numerical artifacts that may arise from an inward-propagating shock hitting the IB in STELLA. Such a cut also can lead to a factor of 10 or more speedup in number of time steps required to produce a light curve.

Appendix B

Extension of the Plateau due to ^{56}Ni Decay

We start with the thermodynamic equation, where a fluid is heated by nuclear decay (in our case, of ^{56}Ni) with complete

⁸ This is controlled by the `star_job` list parameter `stella_skip_inner_v_limit`, which is the minimum velocity of the inner ejecta to include in the profile handed off to STELLA in units of cm s^{-1} .

trapping

$$TdS = dE + PdV = L_{\text{nuc}} dt. \quad (26)$$

In a one-zone, radiation-dominated regime, we can express $P = E/3V$ and $V = 4\pi (vt)^3/3$. Assuming homology, $dV/V = 3dt/t$, and this becomes

$$\frac{1}{t} d(Et) = L_{\text{nuc}} dt. \quad (27)$$

To find the total energy at time t , integrate from from t_{SB} to obtain

$$E(t) = E_0 \frac{t_{\text{SB}}}{t} + \frac{1}{t} \int_{t_{\text{SB}}}^t t' L_{\text{nuc}} dt', \quad (28)$$

where L_{nuc} is due to the $^{56}\text{Ni} \rightarrow ^{56}\text{Co} \rightarrow ^{56}\text{Fe}$ decay chain, following Nadyozhin (1994):

$$L_{\text{nuc}} = \frac{N_{\text{Ni}} Q_{\text{Ni}}}{\tau_{\text{Ni}}} \exp\left(\frac{-t}{\tau_{\text{Ni}}}\right) + \frac{N_{\text{Ni}} Q_{\text{Co}}}{\tau_{\text{Co}} - \tau_{\text{Ni}}} \left[\exp\left(\frac{-t}{\tau_{\text{Co}}}\right) - \exp\left(\frac{-t}{\tau_{\text{Ni}}}\right) \right], \quad (29)$$

where $N_{\text{Ni}} = M_{\text{Ni}}/(56 \text{ amu})$, τ_X is the lifetime of radioactive species X, and Q_X is the energy per decay of species X.

Assuming that only ^{56}Ni is produced in the explosion and all ^{56}Co comes from ^{56}Ni decay, the contribution to the internal energy due to the ^{56}Ni decay chain over the lifetime of the SN is

$$E_{\text{tot, Ni}} = \frac{1}{t_p} \int_{t_{\text{SB}}}^{t_p} t L_{\text{nuc}} dt. \quad (30)$$

We now make a few approximations: First, by the end of the plateau, ^{56}Ni has undergone many decay times. Thus, we take $t_{\text{SB}} \rightarrow 0$ and $t_p/\tau_{\text{Ni}} \rightarrow \infty$ when in the bounds of our integrals. However, the decay time of ^{56}Co is 111.3 days, which is comparable to t_p . Thus, we approximate $t_p/\tau_{\text{Co}} \approx 1$ when in the bounds of our integrals. Outside the integrals, we assume that the time to shock breakout is roughly the expansion time, $t_{\text{SB}} \approx t_e$, where, as in Section 3,

$$t_e = R_0/v_e, \\ v_e = \sqrt{\frac{2E_{\text{exp}}}{M_{\text{ej}}}} \approx 3.16 \times 10^8 M_{10} E_{51} \text{ cm s}^{-1}.$$

Any numerical quantities are, in reality, dependent on the specifics of the relevant timescales. Here we aim primarily to capture the relevant scaling relationships, fitting against our models to find appropriate numerical prefactors.

Computing these integrals and simplifying, we find that

$$E_{\text{int}}(t_p) = \frac{E_0 t_e}{t_p} + \frac{N_{\text{Ni}}}{t_p} \left[Q_{\text{Ni}} \tau_{\text{Ni}} + Q_{\text{Co}} \left(\frac{0.26 \tau_{\text{Co}}^2 - \tau_{\text{Ni}}^2}{\tau_{\text{Co}} - \tau_{\text{Ni}}} \right) \right] \quad (31)$$

$$= \frac{E_0 t_e}{t_p} \times f_{\text{rad}}, \text{ where} \quad (32)$$

$$f_{\text{rad}} \equiv 1 + \frac{N_{\text{Ni}}}{t_e E_0} (Q_{\text{Ni}} \tau_{\text{Ni}} + Q_{\text{Co}} \tau'_{\text{Co}}) \text{ and} \quad (33)$$

$$\tau'_{\text{Co}} \equiv \left(\frac{0.26 \tau_{\text{Co}}^2 - \tau_{\text{Ni}}^2}{\tau_{\text{Co}} - \tau_{\text{Ni}}} \right), \quad (34)$$

noting that E_0 , the internal energy at t_{SB} , is roughly half the total energy of the explosion (mentioned as a comment in K&W); we set $E_0 = E_{\text{exp}}/2$.

We can reexpress f_{rad} as

$$f_{\text{rad}} = 1 + \frac{M_{\text{Ni}}}{E_0} \frac{\tau_{\text{Ni}}}{t_e} \left(q_{\text{Ni}} + q_{\text{Co}} \frac{\tau'_{\text{Co}}}{\tau_{\text{Ni}}} \right), \quad (35)$$

where q_X is the specific (per gram) energy released by the decay of species X; in this case $q_X = Q_X/56 \text{ amu}$.

Following Nadyozhin (1994), we use $Q_{\text{Ni}} = 1.75 \text{ MeV nucleon}^{-1}$, $Q_{\text{Co}} = 3.73 \text{ MeV nucleon}^{-1}$, $\tau_{\text{Ni}} = 8.8 \text{ days}$, and $\tau_{\text{Co}} = 111.3 \text{ days}$. We thus find that

$$f_{\text{rad}} \approx 1 + 7.0 (M_{\text{Ni}, \odot} E_{51}^{-1/2} R_{500}^{-1} M_{10}^{-1/2}). \quad (36)$$

This argument ignores the effects of the distribution of ^{56}Ni , as we necessarily have assumed in this simple one-zone model that the nickel is distributed evenly throughout the ejecta. If the heat from the ^{56}Ni decay is trapped inside the core of the star until that material becomes optically thin, then this would further extend the duration of the plateau. Thus, we should treat the factor of 7.0 as a rough lower bound, rather than an expectation.

We can also recast Equation (36) in terms of ET and η_{Ni} . Although our derivation assumes that all internal energy is trapped to be radiated away, and the Shussman et al. (2016a) derivation of ET assumes that all energy is radiated away, this is just a difference in terms and not a difference in physics. Thus, at $t = t_p$, plugging in $ET = E_0 t_{\text{SB}} \approx E_0 t_e$ and $\eta_{\text{Ni}} = \left(\int_{t_{\text{SB}}}^{t_p} t L_{\text{nuc}} dt \right) / ET$ to Equation (28), we recover

$$E_{\text{int}}(t_p) = E_0 \frac{t_e}{t_p} + \frac{ET \eta_{\text{Ni}}}{t_p} \approx \frac{E_0 t_e}{t_p} (1 + \eta_{\text{Ni}}), \quad (37)$$

so $f_{\text{rad}} \approx 1 + \eta_{\text{Ni}}$.

ORCID iDs

Jared A. Goldberg  <https://orcid.org/0000-0003-1012-3031>

References

- Arnett, W. D. 1980, *ApJ*, **237**, 541
 Baklanov, P. V., Blinnikov, S. I., & Pavlyuk, N. N. 2005, *AsL*, **31**, 429
 Bellm, E. C., Kulkarni, S. R., Graham, M. J., et al. 2019, *PASP*, **131**, 018002
 Bersten, M. C., & Hamuy, M. 2009, *ApJ*, **701**, 200
 Blinnikov, S., & Sorokina, E. 2004, *Ap&SS*, **290**, 13
 Blinnikov, S. I., Eastman, R., Bartunov, O. S., Popolitov, V. A., & Woosley, S. E. 1998, *ApJ*, **496**, 454
 Blinnikov, S. I., Röpke, F. K., Sorokina, E. I., et al. 2006, *A&A*, **453**, 229
 Brayton, R. K., Gustavson, F. G., & Hachtel, G. D. 1972, *IEEEP*, **60**, 98
 Brown, T. M., Baliber, N., Bianco, F. B., et al. 2013, *PASP*, **125**, 1031
 Burrows, A., Radice, D., & Vartanyan, D. 2019, *MNRAS*, **485**, 3153
 Castor, J. I. 1970, *MNRAS*, **149**, 111
 Chugai, N. N. 1991, *SvAL*, **17**, 210
 Dessart, L., & Hillier, D. J. 2019, arXiv:1903.04840
 Dessart, L., Hillier, D. J., Waldman, R., & Livne, E. 2013, *MNRAS*, **433**, 1745
 Duffell, P. C. 2016, *ApJ*, **821**, 76
 Gear, C. W. 1971, *Numerical Initial Value Problems in Ordinary Differential Equations* (Englewood Cliffs, NJ: Prentice-Hall)
 Gutiérrez, C. P., Anderson, J. P., Hamuy, M., et al. 2017, *ApJ*, **850**, 90
 Hamuy, M. 2003, *ApJ*, **582**, 905
 Hunter, J. D. 2007, *CSE*, **9**, 90

- Jerkstrand, A., Fransson, C., Maguire, K., et al. 2012, *A&A*, **546**, A28
- Jones, E., Oliphant, T., Peterson, P., et al. 2001, SciPy: Open Source Scientific Tools for Python, <https://www.scipy.org>
- Kasen, D., Thomas, R. C., & Nugent, P. 2006, *ApJ*, **651**, 366
- Kasen, D., & Woosley, S. E. 2009, *ApJ*, **703**, 2205
- Kluyver, T., Ragan-Kelley, B., Pérez, F., et al. 2016, in Positioning and Power in Academic Publishing: Players, Agents and Agendas, ed. F. Loizides & B. Schmidt (Amsterdam: IOS Press), 87
- Kochanek, C. S., Shappee, B. J., Stanek, K. Z., et al. 2017, *PASP*, **129**, 104502
- Kozyreva, A., Nakar, E., & Waldman, R. 2018, *MNRAS*, **483**, 1211
- Lisakov, S. M., Dessart, L., Hillier, D. J., Waldman, R., & Livne, E. 2017, *MNRAS*, **466**, 34
- Litvinova, I. Y., & Nadyozhin, D. K. 1983, *Ap&SS*, **89**, 89
- LSST Science Collaboration, Abell, P. A., Allison, J., et al. 2009, arXiv:0912.0201
- Mihalas, D. 1978, *Stellar Atmospheres* (2nd ed.; San Francisco, CA: Freeman), 650
- Morozova, V., Piro, A. L., Renzo, M., & Ott, C. D. 2016, *ApJ*, **829**, 109
- Morozova, V., Piro, A. L., & Valenti, S. 2017, *ApJ*, **838**, 28
- Müller, T., Prieto, J. L., Pejcha, O., & Clocchiatti, A. 2017, *ApJ*, **841**, 127
- Nadyozhin, D. K. 1994, *ApJS*, **92**, 527
- Nakar, E., Poznanski, D., & Katz, B. 2016, *ApJ*, **823**, 127
- Paxton, B., Bildsten, L., Dotter, A., et al. 2011, *ApJS*, **192**, 3
- Paxton, B., Cantiello, M., Arras, P., et al. 2013, *ApJS*, **208**, 4
- Paxton, B., Marchant, P., Schwab, J., et al. 2015, *ApJS*, **220**, 15
- Paxton, B., Schwab, J., Bauer, E. B., et al. 2018, *ApJS*, **234**, 34
- Paxton, B., Smolec, R., Gaudy, A., et al. 2019, *ApJS*, in press(arXiv:1903.01426)
- Pejcha, O., & Prieto, J. L. 2015a, *ApJ*, **799**, 215
- Pejcha, O., & Prieto, J. L. 2015b, *ApJ*, **806**, 225
- Pérez, F., & Granger, B. E. 2007, *CSE*, **9**, 21
- Perna, R., Duffell, P., Cantiello, M., & MacFadyen, A. I. 2014, *ApJ*, **781**, 119
- Popov, D. V. 1993, *ApJ*, **414**, 712
- Shussman, T., Nakar, E., Waldman, R., & Katz, B. 2016a, arXiv:1602.02774
- Shussman, T., Waldman, R., & Nakar, E. 2016b, 05323, arXiv:1610.05323
- Smartt, S. J. 2009, *ARA&A*, **47**, 63
- Smartt, S. J. 2015, *PASA*, **32**, e016
- Sobolev, V. V. 1960, *Moving Envelopes of Stars* (Cambridge, MA: Harvard Univ. Press)
- Sukhbold, T., Ertl, T., Woosley, S. E., Brown, J. M., & Janka, H.-T. 2016, *ApJ*, **821**, 38
- Utrobin, V. P. 2007, *A&A*, **461**, 233
- Utrobin, V. P., Wongwathanarat, A., Janka, H.-T., & Müller, E. 2017, *ApJ*, **846**, 37
- Valenti, S., Howell, D. A., Stritzinger, M. D., et al. 2016, *MNRAS*, **459**, 3939
- van der Walt, S., Colbert, S. C., & Varoquaux, G. 2011, *CSE*, **13**, 22
- Wolf, B., Bauer, E. B., & Schwab, J. 2017, wmwolf/MesaScript: A DSL for Writing MESA Inlists
- Wolf, B., & Schwab, J. 2017, wmwolf/py_mesa_reader: Interact with MESA Output
- Wongwathanarat, A., Müller, E., & Janka, H.-T. 2015, *A&A*, **577**, A48
- Woosley, S. E., & Weaver, T. A. 1988, *PhR*, **163**, 79